Title

Charge-Transfer Plasmon Polaritons at Graphene/α-RuCl3 Interfaces

Journal

Nano Letters, 20(12)

ISSN

1530-6984

Authors

Rizzo, Daniel J
Jessen, Bjarke S
Sun, Zhiyuan
et al.

Publication Date

2020-12-09

DOI

10.1021/acs.nanolett.0c03466

NANO LETTERS

pubs.acs.org/NanoLett Letter

Charge-Transfer Plasmon Polaritons at Graphene/α-$RuCl_3$ Interfaces

Daniel J. Rizzo, Bjarke S. Jessen, Zhiyuan Sun, Francesco L. Ruta, Jin Zhang, Jia-Qiang Yan, Lede Xian, Alexander S. McLeod, Michael E. Berkowitz, Kenji Watanabe, Takashi Taniguchi, Stephen E. Nagler, David G. Mandrus, Angel Rubio, Michael M. Fogler, Andrew J. Millis, James C. Hone, Cory R. Dean, and D. N. Basov*

Cite This: https://dx.doi.org/10.1021/acs.nanolett.0c03466 Read Online

ACCESS | Metrics & More | Article Recommendations | Supporting Information

ABSTRACT: Nanoscale charge control is a key enabling technology in plasmonics, electronic band structure engineering, and the topology of two-dimensional materials. By exploiting the large electron affinity of α-$RuCl_3$, we are able to visualize and quantify massive charge transfer at graphene/α-$RuCl_3$ interfaces through generation of charge-transfer plasmon polaritons (CPPs). We performed nanoimaging experiments on graphene/α-$RuCl_3$ at both ambient and cryogenic temperatures and discovered robust plasmonic features in otherwise ungated and undoped structures. The CPP wavelength evaluated through several distinct imaging modalities offers a high-fidelity measure of the Fermi energy of the graphene layer: E_F = 0.6 eV (n = 2.7 × 10^{13} cm^{-2}). Our first-principles calculations link the plasmonic response to the work function difference between graphene and α-$RuCl_3$ giving rise to CPPs. Our results provide a novel general strategy for generating nanometer-scale plasmonic interfaces without resorting to external contacts or chemical doping.

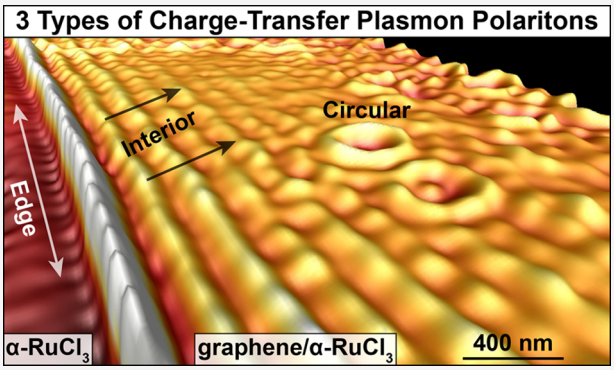

KEYWORDS: *plasmon polaritons, α-$RuCl_3$, graphene, scanning near-field optical microscopy (SNOM), two-dimensional (2D) materials, Mott insulators*

INTRODUCTION

Research in two-dimensional (2D) materials has generated a library of tailor-made atomically thin layers whose optoelectronic properties are dictated by their lattice symmetry and elemental composition. The behavior of 2D materials can be further controlled via chemical or electrostatic doping.[1,2] Moreover, van der Waals (vdW) heterostructures show emergent behavior based on interfacial effects, including orbital hybridization,[3−5] magnetic interactions,[6] and proximal superconductivity.[7] Work function-mediated interlayer charge transfer offers another route to realizing novel interfacial phenomena.[8−11] Specifically, the large work function of α-$RuCl_3$ (Φ_{RuCl3} = 6.1 eV)[8] compared to graphene (Φ_g = 4.6 eV)[12] is predicted to prompt interlayer charge transfer that creates in excess of n = 10^{13} cm^{-2} holes and electrons in graphene and α-$RuCl_3$, respectively. Such large charge carrier densities will likely impact the correlated insulating ground state of α-$RuCl_3$.[13−18] Simultaneously, this interlayer charge transfer should metalize graphene, giving rise to plasmon polaritons without the need of electrical contacts or chemical alteration (as required previously), herein called charge-transfer plasmon polaritons (CPPs) (distinct from similarly named effects in coupled metallic nanoparticles).[19] These hybrid light-matter modes formed by infrared photons and Dirac electrons can travel over macroscopic distances in structures with high mobility.[20−22]

Here, we harness CPPs to visualize and quantify charge transfer at the graphene/α-$RuCl_3$ interface. The CPP wavelength is dictated by the electron density in the host medium, allowing us to read the strength of the charge transfer and the associated Fermi energy (E_F) in graphene/α-$RuCl_3$ heterostructures directly from CPP images. The totality of CPP imaging data allows us to map the nanoscale spatial dependence of the interlayer charge transfer throughout the graphene/α-$RuCl_3$ interface. Moreover, the electric field of the polaritonic wave extends over tens of nanometers outside of the graphene plane and provides access to the charge dynamics in effectively doped α-$RuCl_3$.

A polaritonic probe of graphene/α-$RuCl_3$ heterostructures is enabled by scattering-type scanning near-field optical microscopy (s-SNOM), which permits us to map the near-field

Received: August 26, 2020
Revised: November 2, 2020

https://dx.doi.org/10.1021/acs.nanolett.0c03466
Nano Lett. XXXX, XXX, XXX−XXX

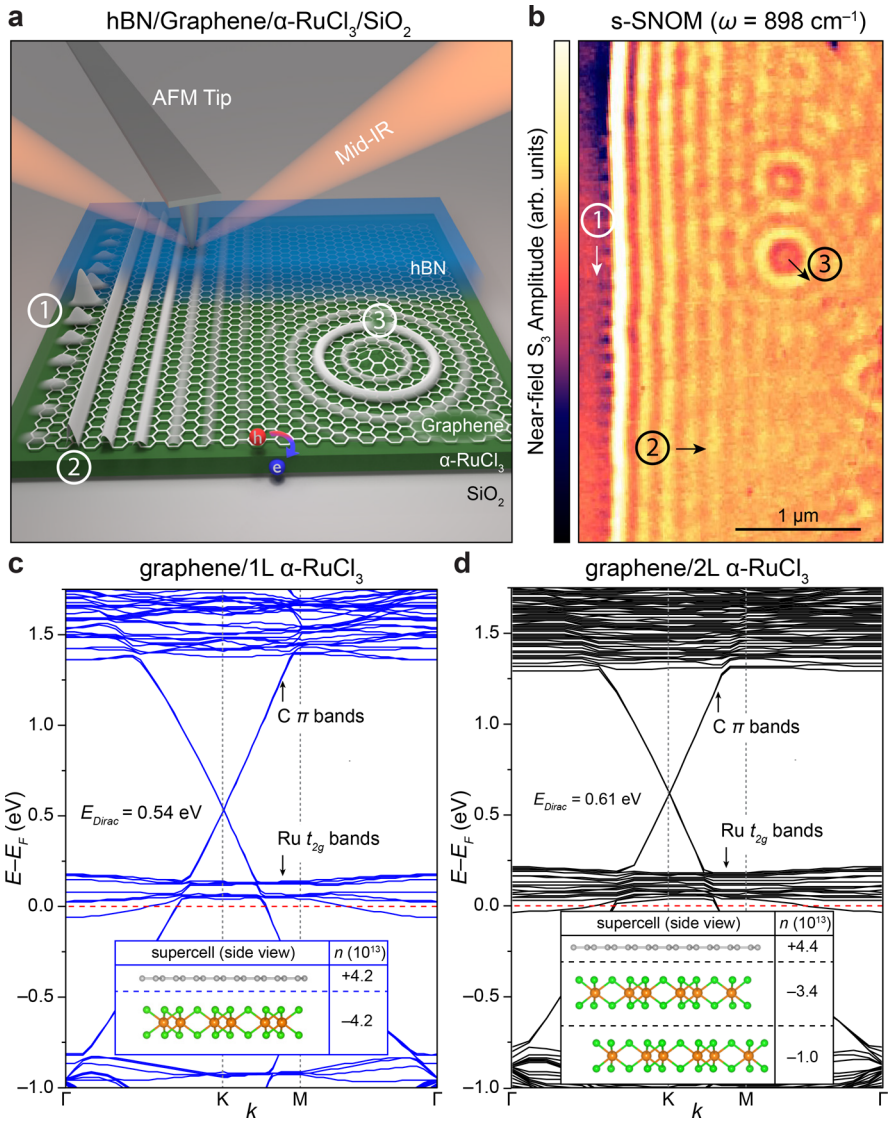

Figure 1. Characterization of interlayer charge transfer in graphene/α-$RuCl_3$ heterostructures using s-SNOM and DFT calculations. (a) Diagram of s-SNOM performed on hBN/graphene/α-$RuCl_3$/SiO_2. The large interlayer charge transfer creates the necessary conditions for generating three types of plasmon features: (1) edge CPPs, (2) CPPs, and (3) circular CPPs. (b) Map of the near-field amplitude near the edge of graphene in hBN/graphene/α-$RuCl_3$/SiO_2 (ω = 898 cm^{-1}, T = 60 K) showing oscillations that are characteristic of the three features shown in (a). (c) First-principles band structure with Hubbard U terms and including spin−orbital coupling for graphene/1L α-$RuCl_3$ (supercell shown in the inset). Bands derived from carbon π-orbitals and Ru t_{2g} orbital are indicated. Inset: The calculated Bader charge in each layer of the model supercell is indicated in terms of the resulting charge carrier concentration, n in units of cm^{-2}. (d) Same as (c) but for graphene/2L α-$RuCl_3$. Here, the interfacial layer of α-$RuCl_3$ possesses >70% of the electrons transferred from graphene.

optical response of this interface at subdiffractional length scales.[23] Thus, s-SNOM is well suited to image CPP waves over a wide range of IR frequencies (here, ω = 900−2300 cm^{-1}). Nanoimaging has allowed us to reconstruct the energy momentum dispersion $\omega(q_1)$ of CPPs prompted by an exceptionally high charge-carrier density in graphene (n = 2.7 × 10^{13} cm^{-2}, E_F = 0.6 eV). Further analyses of both edge and circular CPPs (defined in Figure 1a,b) provide additional insight into the nanoscale spatial dependence of interlayer charge transfer and reveal sharp boundaries in the local optical conductivity. Finally, we evaluated the response function of doped α-$RuCl_3$ by modeling the complex CPP wavevector $\mathbf{q}$ = $\mathbf{q}_1$ + $i\mathbf{q}_2$ and its variation with frequency and temperature. Here, $\mathbf{q}_1$ encodes information about the plasmon wavelength ($\lambda_p = 2\pi/\mathbf{q}_1$), while $\mathbf{q}_2$ characterizes the plasmon damping. We observe CPP scattering that is consistent with an emergent electronic response in the topmost layer of doped α-$RuCl_3$ at infrared frequencies deep below its band gap. DFT analysis confirms that it is primarily the interfacial layer of α-$RuCl_3$ that is impacted by charge transfer.

SEEING CHARGE-TRANSFER PLASMON POLARITONS

In order to explore the charge dynamics of the graphene/α-$RuCl_3$ interface, we first constructed a graphene/α-$RuCl_3$ heterostructure on a SiO_2/Si substrate encapsulated with hexagonal boron nitride (hBN) as shown in Figure 1a (see Supporting Information and Figure S1 for assembly details). Nano-IR images for graphene/α-$RuCl_3$ heterostructures reveal three distinct but related forms of polaritonic waves (Figure 1b). Here, oscillations in the near-field amplitude are observed propagating inward from the graphene boundary that are

https://dx.doi.org/10.1021/acs.nanolett.0c03466
Nano Lett. XXXX, XXX, XXX−XXX

characteristic of CPPs. We also observe CPP fringes emanating radially from pointlike (r < 50 nm, $h \sim 1$ nm) topographic defects that appear to be acting as local plasmon reflectors, herein referred to as circular CPPs. Finally, we observed edge CPP fringes oscillating along the graphene edge. For pristine graphene, the plasmon wavelength, $\lambda_p \sim E_F^{-1/2}$, and can be used as a rough but straightforward measure of the interlayer charge transfer.[24] Here, all three imaging modalities produce a consistent estimate of E_F = 0.5−0.6 eV induced by charge transfer. Self-consistent DFT+U calculations on isolated α-$RuCl_3$ (Figure S2) and two heterostructures containing one (1L) and two (2L) layers of α-$RuCl_3$ (Figure 1c,d) yield similarly large values of E_F relative to that of pristine graphene (0.54 and 0.61 eV, respectively). Together, these observations reveal that the work function difference between graphene and α-$RuCl_3$ is sufficient to provide the conditions for generating prominent CPPs and potentially dope interfacial α-$RuCl_3$ into new physical regimes.

QUANTIFYING INTERFACIAL CHARGE DYNAMICS WITH CPPS

We proceed with our quantitative analysis of the CPP fringes visualized over a wide range of frequencies in the mid-IR using s-SNOM (Figure 2a,b). No such fringes were observed for graphene residing directly on SiO_2 (Figure S3), suggesting that this behavior originates from the graphene/α-$RuCl_3$ interface. The CPP wavelength reveals a systematic variation with the incident laser frequency, ω, uncovering the dispersion $\omega(q_1)$ of these modes (Figure 2b). By fitting the average line profile of the CPP fringes (Figure S4),[21,25] we are able to extract the dispersion for CPPs at the graphene/α-$RuCl_3$ interface (Figure 2c). The experimental dispersion shows two branches: a lower branch in the frequency range 900−1010 cm^{-1} and an upper branch spanning 1380−2300 cm^{-1}; the two branches are separated by a region of SiO_2 and hBN phonons, in accord with prior results.[26]

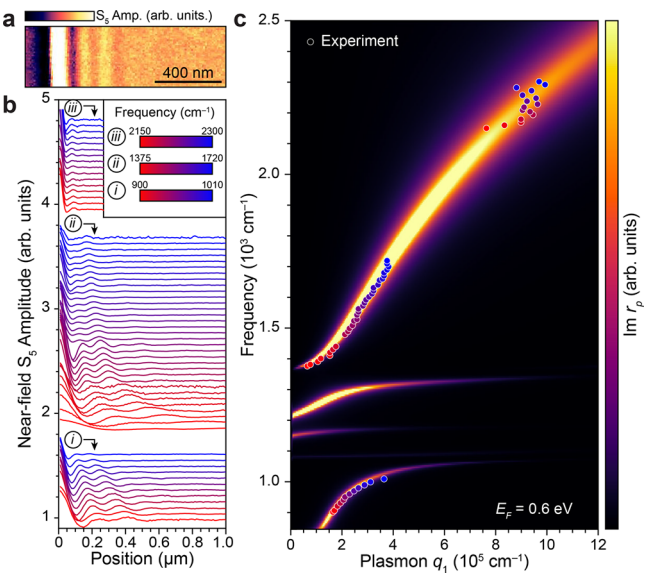

Figure 2. Characterization of the CPP dispersion in graphene/α-$RuCl_3$ heterostructures using s-SNOM. (a) Map of the near-field amplitude (ω = 960 cm^{-1}) near a graphene edge in graphene/α-$RuCl_3$, showing CPP fringes. (b) Line profiles of the average near-field amplitude as a function of distance from the graphene edge for ω = 900−2300 cm^{-1}, showing substantial shifts in the CPP wavelength. Here, sequential curves are offset vertically by 0.1 for clarity and grouped based on the three different ranges of frequencies labeled in the inset. (c) Dots: Plots of the experimental CPP dispersion derived from fits to the line profiles shown in (b) (Figure S4). The experimental data is superimposed on our best-fit theoretical model of Im r_p, with E_F = 0.6 eV.

An evident novelty of the data shown in Figure 2 is that the CPP dispersion is achieved without resorting to either gating or chemical doping. The appearance of CPP fringes in graphene/α-$RuCl_3$ therefore attests to substantial charge transfer between graphene and α-$RuCl_3$. We are able to refine our extraction of E_F (i.e., the interlayer charge transfer) from the CPP behavior by modeling the precise dielectric environment of the graphene. Specifically, we calculate the theoretical plasmon dispersion from the p-polarized Fresnel reflection coefficient (r_p) and compared it to the experimental $\omega(q_1)$ plasmon dispersion. Our model properly accounts for the response functions and thicknesses of all constituent layers in the encapsulated graphene/α-$RuCl_3$ heterostructure as described in the Supporting Information. Multilayer calculations of Im r_p validate that the dominant contribution to the nano-optical response originates from plasmons in the graphene layer. A least-squares regression between the experimental dispersion and maxima in Im r_p yields the graphene E_F as a fitting parameter (Figures 2c, S5). The model captures all of the trends in the data with the best-fit value of E_F = 0.6 eV corresponding to $n = 2.7 \times 10^{13}$ cm^{-2} carriers in the graphene layer due to interlayer charge transfer (Figure 2c). This value is consistent with previous measurements of the Hall resistance ($n = 2.8 \times 10^{13}$ cm^{-2})[8] and is in good agreement with theoretical expectation (Figure 1c,d).[27] We note that the agreement between the experimental and model dispersions was improved by assuming that the topmost layer of α-$RuCl_3$ possesses additional optical conductivity (Figure S5) compared to that of undoped α-$RuCl_3$.[28] Hence, our data establish the notion of large interfacial doping and enhanced optical conductivity in α-$RuCl_3$ as suggested by DFT calculations (Figure 1c,d).

While graphene/α-$RuCl_3$ CPP fringes were primarily observed launching and reflecting from the graphene boundary, the interior of graphene reveals a different type of plasmonic oscillations exactly centered around topographic point defects (Figure S6a,b). We posit that these latter circular CPPs reflect off of these defects, forming radially symmetric $\lambda_p/2$ fringe patterns in the near-field amplitude. The lack of additional λ_p modulations to the circular CPP fringe pattern suggests that defects only act as reflectors of polaritonic waves but not as launchers. Detailed modeling corroborates this intuition (see Supporting Information for more details). Here, the defect is described as a small ($r \sim 40$ nm) region with a variable conductivity relative to the uniform areas in the interior of the sample (Figure S6c,d), while the near-field amplitude is approximated by a position-dependent reflectivity for illuminating fields from a raster-scanned point dipole. We observe that the sign and magnitude of the primary circular CPP fringe depend on the defect conductivity relative to that of the surrounding graphene. Conductivity-excess defects show a bright primary fringe, while conductivity-depletion defects show a dark primary fringe. A good fit to the experimental fringe cross-section can only be achieved with a maximally depleted (i.e., nonconducting) region at the defect site. Indeed, all defects in our data produce a dark primary fringe, consistent with the notion of depleted conductivity at the defect site. The

https://dx.doi.org/10.1021/acs.nanolett.0c03466
Nano Lett. XXXX, XXX, XXX−XXX

circular CPPs follow a dispersion that is similar to that of Figure 2c in the overlapping frequency region, implying that a similarly high level of hole density rapidly builds up away from the defect site (Figure S6e). Therefore, the near-field behavior of topographic defects reveals that they are sharp (nanometer-scale) undoped features surrounded by heavily doped graphene, consistent with a nanobubble in the graphene/α-$RuCl_3$ interface.

The magnitude and spatial-dependence of the interlayer charge transfer between graphene and α-$RuCl_3$ revealed by s-SNOM experiments is further corroborated by Raman spectroscopy (Figure S7). Here, analysis of the graphene G and 2D peak shifts shows the coexistence of a highly doped ($n = 2.5 \times 10^{13}$ cm^{-2}), uniformly strained ($\varepsilon = -0.2\%$) phase, and an undoped, randomly strained phase. The latter undoped phase only appears to be substantially represented in regions observed to have a high density of point defects (Figure S7).

Although bulk CPP dispersions act as sensitive probes of the interlayer charge transfer in the graphene interior, the edge CPP dispersion can provide information about the charge transfer profile near the boundary of graphene.[29] In order to exploit this, we extract the profiles of the near-field oscillations along the graphene edge as a function of ω (Figure 3a). The latter profiles correspond to $\lambda_p/2$ fringes generated by tip-launched edge CPPs reflecting off of notches in the graphene edge (Figures 3a, S4). As with the CPP fringes, the wavelength of the edge CPPs has a clear dependence on ω as shown in Figure 3b. As expected,[30−32] edge CPPs possess a systematically higher value of $\mathbf{q}_1$ compared to CPPs in the interior (Figure 3b). Following the procedure in ref 29, we model the edge CPP dispersion based on the assumption of an abrupt boundary in the graphene conductivity coinciding with the graphene edge. This shows good agreement with experiment (Figure 3b). We remark that edge plasmons in graphene are a relatively rare sighting as they are likely to be smeared by electric field fringing in structures with relatively thick gate insulators and they have previously suffered dephasing when scattered by edge roughness.

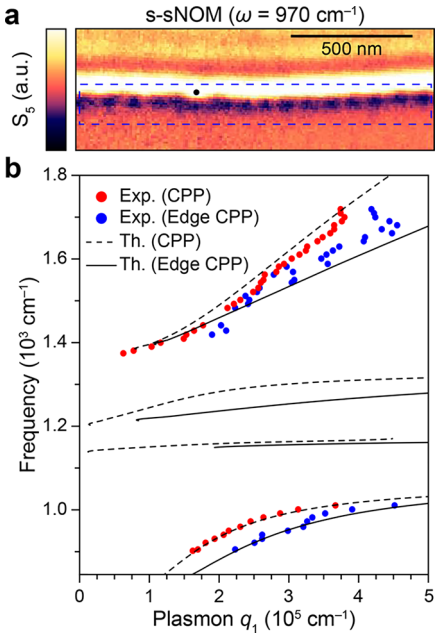

Figure 3. Analysis of the edge CPP dispersion in graphene/α-$RuCl_3$ heterostructures. (a) Characteristic s-SNOM image (ω = 970 cm^{-1}) of edge CPP fringes along the graphene edge (highlighted by the dashed blue box). The fringe pattern shows $\lambda_p/2$ standing-waves formed by tip-launched edge plasmons reflecting off of notches in the graphene edge (such as that denoted by the solid black circle). (b) Red dots: The low-frequency CPP dispersion reproduced from Figure 2c. Blue dots: The edge CPP dispersion extracted from line profiles of the near-field amplitude along the graphene edge (see Figure S4). The dashed (solid) line shows the expected CPP (edge CPP) dispersion based on the assumption of a discontinuous jump in the graphene conductivity along that graphene edge (see Supporting Information).

EMERGENT ELECTRONIC RESPONSE OF INTERFACIAL α-RUCL$_3$

In order to accurately account for the depth of interlayer charge transfer in our modeling of the graphene/α-$RuCl_3$ optical response, we revisit the first-principles calculations shown in Figure 1c,d. Analysis of the Bader charge[33] of both 1L and 2L structures shows that the graphene is heavily doped regardless of the number of α-$RuCl_3$ layers in our heterostructures. In principle, the graphene-α-$RuCl_3$ charge transfer can be tuned with the incorporation of hBN spacer layers (Figure S2). At the same time, the interfacial layer of α-$RuCl_3$ is nearly as heavily doped in the 2L structure as it is in the 1L structure (0.069 versus 0.056 $|e|$/Ru atom, respectively), while the second layer of α-$RuCl_3$ receives <30% of the electrons of the first (Figure 1c,d). Therefore, only the topmost interfacial layer of α-$RuCl_3$ is sufficiently doped to experience significant changes of the optoelectronic response, while subsequent layers more closely resemble the undoped bulk electronic structure. For every theoretical graphene/α-$RuCl_3$ heterostructure characterized in our study, Ru t_{2g} bands that are unoccupied in intrinsic α-$RuCl_3$ (Figure S2) become populated, raising the possibility of emergent metallicity in α-$RuCl_3$ doped via interlayer charge transfer. With this in mind, all models of the optical response of our stack presented in this text consider the possibility of emergent optical conductivity in the topmost layer of α-$RuCl_3$ (Figure S8).

We evaluate the optical response of the graphene/α-$RuCl_3$ interface by comparing the experimentally derived plasmon quality factor to all known loss channels. The inverse of the CPP quality factor, Q^{-1}, can be expressed in terms of the effective dielectric environment[20] and the optical conductivity of the graphene/α-$RuCl_3$ interface

$$Q^{-1} = \frac{q_2}{q_1} \approx \frac{\sigma_1}{\sigma_2} + \frac{\kappa_2}{\kappa_1} = \frac{\gamma(\omega)}{\omega} + \frac{\kappa_2}{\kappa_1} \quad (1)$$

where $\sigma = \sigma_1 + i\sigma_2$ is the complex optical conductivity of the graphene/α-$RuCl_3$ interface and $\kappa = \kappa_1 + i\kappa_2$ is the effective dielectric of the environment of our stack excluding the interfacial graphene/α-$RuCl_3$ layers. The frequency-dependent scattering rate ($\gamma(\omega)$) has additive components, which can be broadly attributed to either the graphene ($\gamma_g(\omega)$) or α-$RuCl_3$ ($\gamma_{\alpha RuCl_3}(\omega)$) side of the interface

$$\gamma(\omega) = \gamma_{\alpha RuCl_3}(\omega) + \gamma_g(\omega) \quad (2)$$

The plasmonic dissipation in graphene, $\gamma_g(\omega)$, is well understood, and at room temperature is dominated by phonons.[20] Pristine α-$RuCl_3$ is a moderate gap insulator with a vanishingly small electronic response at infrared frequencies and does not significantly impact plasmonic losses. Conceivably, additional scattering may emerge as a result of a nontrivial electronic response at the interfacial layer of α-$RuCl_3$, which in

https://dx.doi.org/10.1021/acs.nanolett.0c03466
Nano Lett. XXXX, XXX, XXX−XXX

turn should lead to a suppression of the experimental Q. With this in mind, we first extract the plasmon quality factor as a function of ω from the experimental fits to the CPP line profiles shown in Figure 2b, revealing a systematic decrease in Q with ω (Figure 4a). Using (1) along with known substrate optical parameters, the experimental Q can be used to obtain the combined scattering rate $\gamma(\omega)$ (Figure 4b). The contribution of graphene phonons to the scattering rate is shown in Figure 4b. Intrinsic scattering mechanisms in graphene fall short of the experimental values, revealing the presence of additional sources of scattering at the graphene/α-$RuCl_3$ interface. While disorder is a potential source of scattering, such channels tend to produce frequency- and temperature-independent losses. The clear frequency dependence of the excess experimental scattering (i.e., beyond what is attributable to graphene) suggests that disorder alone does not offer an adequate description. Thus, we attribute the excess temperature- and frequency-dependent losses to emergent optical conductivity in the interfacial α-$RuCl_3$ altered by charge transfer. Our scattering analysis yields Re $\sigma_{\alpha RuCl_3}$ for the topmost layer of α-$RuCl_3$ in the range 0.02−0.1 $e^2/\hbar$ (Figure 4b,c). The small values of the extracted AC conductivity within the experimental frequency window suggest that interrogation of graphene/α-$RuCl_3$ interfaces at lower frequencies is necessary to completely characterize the nature of the electronic response in doped α-$RuCl_3$ (i.e., fully localized versus itinerant charges). Nevertheless, the addition of an α-$RuCl_3$ loss channel greatly improves agreement between the theoretical and experimental scattering rates and quality factors (Figure 4a,b). The totality of these observations provides evidence that doped α-$RuCl_3$ possesses a nontrivial electronic response at infrared frequencies that acts as a damping mechanism for CPPs at the graphene side of the interface.

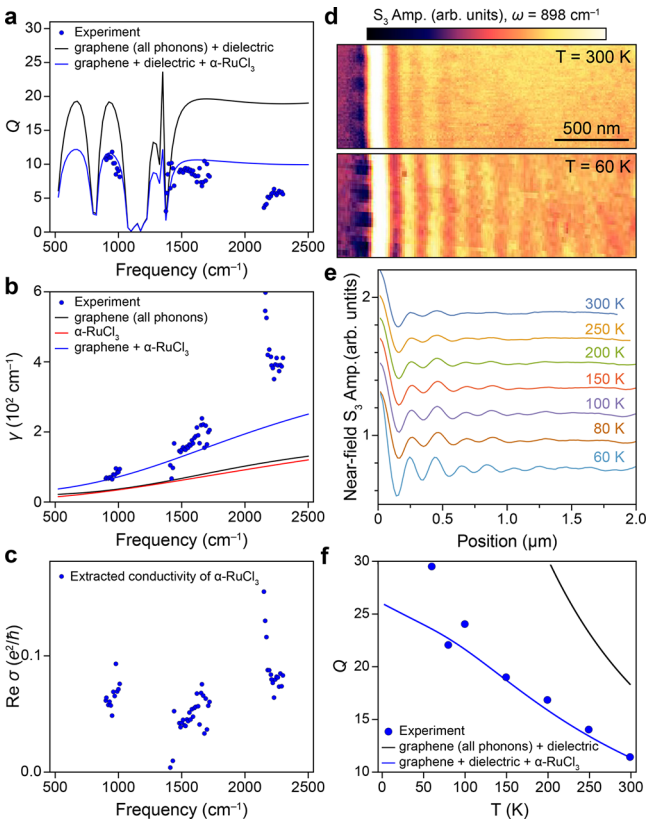

Figure 4. Temperature- and frequency-dependence of CPP losses in graphene/α-$RuCl_3$ heterostructures. (a) Blue dots: Extracted quality factor, Q, for CPPs versus frequency. Black line: model Q versus ω for graphene phonon scattering and the dielectric environment only. Blue line: Same as the black line, plus model losses to the interfacial α-$RuCl_3$ layer. (b) Blue dots: The extracted γ versus ω derived from the experimental data in (a). Black line: The model γ versus ω based on graphene phonon scattering only. Red line: The model interfacial α-$RuCl_3$ scattering rate. Blue line: The total frequency-dependent scattering of the graphene and α-$RuCl_3$ layers. (c) The extracted optical conductivity of interfacial α-$RuCl_3$ based on the excess scattering observed in (b). (d) Map of the near-field amplitude (ω = 898 cm^{-1}) near a graphene edge in graphene/α-$RuCl_3$ heterostructures taken at 300 K (top panel) and 60 K (bottom panel) under ultrahigh vacuum (UHV) conditions. (e) Line profiles of the average near-field amplitude as a function of distance from the graphene edge taken at the indicated sample temperatures ranging from 60−300 K. (f) Blue dots: The extracted CPP Q versus temperature taken from fits to the line profiles in (e) (see Figure S4). Black line: the model temperature-dependent Q based on graphene phonons and dielectric losses only. Blue line: Same as the black line, plus losses to the interfacial α-$RuCl_3$. For (a,f), the additional dielectric refers to losses attributable to all noninterfacial layers of the experimental stack shown in Figure S8 (i.e., the encapsulating hBN, bulk (undoped) α-$RuCl_3$ layers, and the underlying SiO_2.

To further test the possibility of an emergent electronic response in doped α-$RuCl_3$, we obtained the temperature dependence (T = 60−300 K) of the CPP damping rate for ω = 898 cm^{-1} (Figures 4d,e). We observe that the Q-factor nearly triples as the sample temperature is brought from 300 K down to 60 K (Figure 4f). Once again, the calculated experimental scattering rate γ (898 cm^{-1},T) is severely underestimated by phonon scattering and dielectric losses alone and is only reconciled with the model once the topmost layer of α-$RuCl_3$ is assumed to be endowed with an electronic response (Figures 4f, S9). The enhanced scattering rate at all observed temperatures therefore suggests the presence of electronic spectral weight at infrared frequencies in doped α-$RuCl_3$. While it was not possible to probe the DC transport of these carriers, a very small value of their AC conductivity suggests that these carriers may be either strongly correlated or localized.

OUTLOOK

The observations and analyses of CPPs presented in this work have broad implications in the study of α-$RuCl_3$, graphene plasmonics, and 2D materials generally. The recognition that massive charge transfer is taking place over macroscopic areas of graphene provides unambiguous validation of the notion that work function-mediated charge transfer can be used to "metallize" 2D materials into new physical regimes not attainable with common alternative methods. In the past, such high charge carrier densities in graphene could only be achieved with ion liquid gel devices, or an additional top-gate layer,[34] which add complexity to devices and forbid detailed surface studies with a scanning probe. Therefore, our experimental system provides a pathway for generating record high charge carrier densities at unobscured interfaces of 2D materials, which can, in principle, be further tuned with an additional backgate.[8,10] Our findings indicate that it is now feasible to significantly dope 2D Mott insulators via work function mediated charge transfer. This is of particular interest for α-$RuCl_3$, which is predicted to host quantum spin liquids.

https://dx.doi.org/10.1021/acs.nanolett.0c03466
Nano Lett. XXXX, XXX, XXX−XXX

Furthermore, the observation that the graphene optical conductivity forms abrupt boundaries wherever the graphene/α-$RuCl_3$ interface is interrupted suggests that α-$RuCl_3$ can be used to imprint nanoscale conductivity features in graphene and possibly other 2D materials without resorting to local back gates.[35] Similarly, patterned α-$RuCl_3$ arrays should offer a superior route to creating the sharp periodic potentials needed to realize graphene photonic crystals in gate-tunable graphene/semiconductor architectures.[8,10,36] Concurrently, we have refined a procedure for probing the nanoscale optical response of 2D heterostructures across interfaces via the exploration of plasmon damping. This latter analysis hints at an enhanced electronic response in our doped interfacial α-$RuCl_3$ that needs to be verified with future direct measurements in the terahertz regime.

METHODS

Crystal Growth and Preparation. The hBN single crystals were grown using the temperature-gradient method using a Ba−BN solvent system. α-$RuCl_3$ crystals were grown by the sublimation of $RuCl_3$ powder sealed in a quartz tube under vacuum. About 1 g of powder was loaded in a quartz tube of 19 mm in outer diameter, 1.5 mm thick, and 10 cm long. The growth was performed in a box furnace. After dwelling at 1060 °C for 6 h, the furnace was cooled to 800 °C at a rate of 4 °C/h. Magnetic and specific heat measurements confirmed that the as-grown pristine crystal orders antiferromagnetically around 7 K. Graphene was derived from exfoliated highly oriented pyrolytic graphite.

Fabrication of Graphene/α-$RuCl_3$ Heterostructures. The assembly of hBN/graphene/α-$RuCl_3$ heterostructures was performed using standard dry-stacking methods.[37,38] Because our near-field experiments require the encapsulating hBN crystal to be relatively thin (∼3 nm), we opted for using a polycarbonate (PC) film on a polydimethylsiloxane (PDMS) support for the assembly. In our experience, the success rate with PC films is significantly higher than poly(propylene carbonate) (PPC) films when working with sub-5 nm 2D crystals.

To pick up the crystals, we manually bring the PC in contact with the SiO_2 substrate at ∼90 °C using a micromanipulator. When the PC film is close (a few tens of micrometers) to the targeted crystal, we slowly increase the temperature to ∼120 °C. As the temperature gradually increases, the thermal expansion allows the PC film to gradually and nondestructively cover the 2D crystals. By slowly lowering the temperature again, we can pick up the 2D crystals as the PC film retracts. This is performed sequentially on hBN and then graphene (Figure S1). The hBN/graphene stack is then positioned on top of the α-$RuCl_3$/SiO_2 to form the final heterostructure. The PC is then heated to 180 °C, which releases the film from the PDMS transfer slide and deposits it on the SiO_2. Finally, the PC film is removed in chloroform overnight.

Scanning Near-field Optical Microscopy. All s-SNOM measurements were performed on hBN-encapsulated graphene/α-$RuCl_3$ on 285 nm SiO_2 on Si. We include a few layers of encapsulating hBN to protect the graphene surface from unwanted doping via atmospheric contaminants, complying with constraints of s-SNOM. The charge-transfer plasmon polariton (CPP) dispersion data was collected under ambient conditions on two commercial Neaspec systems using continuous wave quantum cascade lasers produced by Daylight Solutions. The temperature dependence of the plasmon damping was measured in a home-built cryogenic s-SNOM using an 11 μm CO_2 laser (Access Laser). s-SNOM experiments were conducted with an AFM operating in noncontact mode using metallic tips. Tapping frequencies of f = 75 and 285 kHz were used for ambient and UHV experiments, respectively. We demodulate the detected signal at the third (S_3) and fifth (S_5) harmonic of the tapping frequency in order to minimize background contributions to the backscattered near-field signal. A pseudoheterodyne interferometer is used to collect concurrent scattering amplitude and phase information from the near-field signal.

Modeling Charge-Transfer Plasmon Polaritons. A detailed description of the modeling employed for CPPs, edge CPPs, and circular CPPs is presented in the Supporting Information.

Ab Initio Calculations of Graphene/α-$RuCl_3$ Heterostructures. The calculations were performed within the Vienna Ab initio Simulation Package (VASP)[39] using a projector-augmented wave (PAW) pseudopotential in conjunction with the Perdew−Burke−Ernzerhof (PBE)[40] functionals and plane-wave basis set with energy cutoff at 400 eV. A detailed description of all ab initio calculations is presented in the Supporting Information.

ASSOCIATED CONTENT

Supporting Information

The Supporting Information is available free of charge at https://pubs.acs.org/doi/10.1021/acs.nanolett.0c03466.

Detailed description of CPP modeling, heterostructure assembly, Raman spectroscopy, supplementary near-field measurements and DFT calculations (PDF)

AUTHOR INFORMATION

Corresponding Author

D. N. Basov − *Department of Physics, Columbia University, New York, New York 10027, United States*; Email: db3056@columbia.edu

Authors

Daniel J. Rizzo − *Department of Physics, Columbia University, New York, New York 10027, United States*; orcid.org/0000-0003-4587-4863

Bjarke S. Jessen − *Department of Physics and Department of Mechanical Engineering, Columbia University, New York, New York 10027, United States*

Zhiyuan Sun − *Department of Physics, Columbia University, New York, New York 10027, United States*

Francesco L. Ruta − *Department of Physics and Department of Applied Physics and Applied Mathematics, Columbia University, New York, New York 10027, United States*; orcid.org/0000-0002-8746-9420

Jin Zhang − *Theory Department, Max Planck Institute for Structure and Dynamics of Matter and Center for Free-Electron Laser Science, 22761 Hamburg, Germany*; orcid.org/0000-0001-7830-3464

Jia-Qiang Yan − *Materials Science and Technology Division, Oak Ridge National Laboratory, Oak Ridge, Tennessee 37831, United States; Department of Materials Science and Engineering, University of Tennessee, Knoxville, Tennessee 37996, United States*

https://dx.doi.org/10.1021/acs.nanolett.0c03466
Nano Lett. XXXX, XXX, XXX−XXX

Lede Xian − *Theory Department, Max Planck Institute for Structure and Dynamics of Matter and Center for Free-Electron Laser Science, 22761 Hamburg, Germany*
Alexander S. McLeod − *Department of Physics, Columbia University, New York, New York 10027, United States*
Michael E. Berkowitz − *Department of Physics, Columbia University, New York, New York 10027, United States;* orcid.org/0000-0001-5962-2857
Kenji Watanabe − *Research Center for Functional Materials, National Institute for Materials Science, Tsukuba 305-0044, Japan;* orcid.org/0000-0003-3701-8119
Takashi Taniguchi − *International Center for Materials Nanoarchitectonics, National Institute for Materials Science, Tsukuba 305-004, Japan;* orcid.org/0000-0002-1467-3105
Stephen E. Nagler − *Neutron Scattering Division, Oak Ridge National Laboratory, Oak Ridge, Tennessee 37831, United States*
David G. Mandrus − *Materials Science and Technology Division, Oak Ridge National Laboratory, Oak Ridge, Tennessee 37831, United States; Department of Materials Science and Engineering, University of Tennessee, Knoxville, Tennessee 37996, United States*
Angel Rubio − *Theory Department, Max Planck Institute for Structure and Dynamics of Matter and Center for Free-Electron Laser Science, 22761 Hamburg, Germany; Center for Computational Quantum Physics, Flatiron Institute, New York, New York 10010, United States; Nano-Bio Spectroscopy Group, Universidad del País Vasco UPV/EHU, San Sebastián 20018, Spain;* orcid.org/0000-0003-2060-3151
Michael M. Fogler − *Department of Physics, University of California San Diego, La Jolla, California 92093, United States*
Andrew J. Millis − *Department of Physics, Columbia University, New York, New York 10027, United States; Center for Computational Quantum Physics, Flatiron Institute, New York, New York 10010, United States*
James C. Hone − *Department of Mechanical Engineering, Columbia University, New York, New York 10027, United States*
Cory R. Dean − *Department of Physics, Columbia University, New York, New York 10027, United States*

Complete contact information is available at: https://pubs.acs.org/10.1021/acs.nanolett.0c03466

Author Contributions

D.J.R. and D.N.B. conceived and performed all near-field and Raman measurements. B.S.J., J.C.H., and C.R.D assembled the heterostructures used for near-field experiments. D.J.R. and B.S.J. collated and analyzed near-field and Raman data. F.L.R performed theoretical analysis of the surface CPP dispersion. Z.S. and A.J.M. performed theoretical analysis of the surface CPP damping rates. J.Z. performed all DFT calculations and analyzed the results with L.X. and A.R. J.-Q.Y., S.E.N., and D.G.M synthesized and characterized α-$RuCl_3$ crystals. A.S.M. and M.E.B performed theoretical modeling of circular plasmons. K.W. and T.T. synthesized and characterized hBN crystals used for encapsulation. M.M.F. performed theoretical analysis of the edge CPP dispersion.

Notes

The authors declare no competing financial interest.

■ ACKNOWLEDGMENTS

Research at Columbia was supported as part of the Energy Frontier Research Center on Programmable Quantum Materials funded by the U.S. Department of Energy (DOE), Office of Science, Basic Energy Sciences (BES), under Award No. DE-SC0019443. J.Z., L.X., and A.R. were supported by the European Research Council (ERC-2015-AdG694097), the Cluster of Excellence "Advanced Imaging of Matter" (AIM) EXC 2056 - 390715994, funding by the Deutsche Forschungsgemeinschaft (DFG, German Research Foundation) under RTG 2247, Grupos Consolidados (IT1249-19) and SFB925 "Light induced dynamics and control of correlated quantum systems". J.Z. acknowledges funding received from the European Union Horizon 2020 research and innovation program under Marie Sklodowska-Curie Grant Agreement 886291 (PeSD-NeSL). J.Z., L.X., and A.R. would like to acknowledge Nicolas Tancogne-Dejean for fruitful discussions and also acknowledge support by the Max Planck Institute-New York City Center for Non-Equilibrium Quantum Phenomena. The Flatiron Institute is a division of the Simons Foundation. D.G.M. acknowledges support from the Gordon and Betty Moore Foundation's EPiQS Initiative, Grant GBMF9069. Work at ORNL was supported by the U.S. Department of Energy, Office of Science, Basic Energy Sciences, Materials Sciences and Engineering Division. K.W. and T.T. acknowledge support from the Elemental Strategy Initiative conducted by the MEXT, Japan, Grant JPMXP0112101001, JSPS KAKENHI Grant JP20H00354, and the CREST (JPMJCR15F3), JST. S.E.N. was supported by the Division of Scientific User Facilities of the U.S. DOE Basic Energy Sciences. M.M.F. acknowledges support from the Office of Naval Research Grant N00014-18-1-2722. D.N.B. is the Vannevar Bush Faculty ONR-VB: N00014-19-1-2630 and Moore investigator in Quantum Materials EPIQS program #9455. A.S.M acknowledges support from award 80NSSC19K1210 under the NASA Laboratory Analysis of Returned Samples program.

■ REFERENCES

(1) Chen, X.; Zhou, Z.; Deng, B.; Wu, Z.; Xia, F.; Cao, Y.; Zhang, L.; Huang, W.; Wang, N.; Wang, L. Electrically tunable physical properties of two-dimensional materials. *Nano Today* **2019**, *27*, 99−119.
(2) Keimer, B.; Moore, J. E. The physics of quantum materials. *Nat. Phys.* **2017**, *13*, 1045−1055.
(3) Mele, E. J. Commensuration and interlayer coherence in twisted bilayer graphene. *Phys. Rev. B: Condens. Matter Mater. Phys.* **2010**, *81*, 161405.
(4) Suarez Morell, E.; Correa, J. D.; Vargas, P.; Pacheco, M.; Barticevic, Z. Flat bands in slightly twisted bilayer graphene: Tight-binding calculations. *Phys. Rev. B: Condens. Matter Mater. Phys.* **2010**, *82*, 121407.
(5) Xian, L.; Kennes, D. M.; Tancogne-Dejean, N.; Altarelli, M.; Rubio, A. Multiflat bands and strong correlations in twisted bilayer boron nitride: Doping-induced correlated insulator and superconductor. *Nano Lett.* **2019**, *19*, 4934−4940.
(6) Zhong, D.; Seyler, K. L.; Linpeng, X.; Cheng, R.; Sivadas, N.; Huang, B.; Schmidgall, E.; Taniguchi, T.; Watanabe, K.; McGuire, M. A.; Yao, W.; Xiao, D.; Fu, K.-M. C.; Xu, X. Van der Waals engineering of ferromagnetic semiconductor heterostructures for spin and valleytronics. *Science Advances* **2017**, *3*, No. e1603113.
(7) Lundeberg, M. B.; Gao, Y.; Asgari, R.; Tan, C.; Van Duppen, B.; Autore, M.; Alonso-González, P.; Woessner, A.; Watanabe, K.; Taniguchi, T.; Hillenbrand, R.; Hone, J.; Polini, M.; Koppens, F. H.

https://dx.doi.org/10.1021/acs.nanolett.0c03466
Nano Lett. XXXX, XXX, XXX−XXX

L. Tuning quantum nonlocal effects in graphene plasmonics. *Science* **2017**, *357*, 187.
(8) Zhou, B.; Balgley, J.; Lampen-Kelley, P.; Yan, J. Q.; Mandrus, D. G.; Henriksen, E. A. Evidence for charge transfer and proximate magnetism in graphene/α-$RuCl_3$ heterostructures. *Phys. Rev. B: Condens. Matter Mater. Phys.* **2019**, *100*, 165426.
(9) Hu, F.; Kim, M.; Zhang, Y.; Luan, Y.; Ho, K. M.; Shi, Y.; Wang, C. Z.; Wang, X.; Fei, Z. Tailored Plasmons in Pentacene/Graphene Heterostructures with Interlayer Electron Transfer. *Nano Lett.* **2019**, *19*, 6058−6064.
(10) Mashhadi, S.; Kim, Y.; Kim, J.; Weber, D.; Taniguchi, T.; Watanabe, K.; Park, N.; Lotsch, B.; Smet, J. H.; Burghard, M.; Kern, K. Spin-Split Band Hybridization in Graphene Proximitized with α-RuCl3 Nanosheets. *Nano Lett.* **2019**, *19*, 4659−4665.
(11) Wang, Y.; Balgley, J.; Gerber, E.; Gray, M.; Kumar, N.; Lu, X.; Yan, J.-Q.; Fereidouni, A.; Basnet, R.; Yun, S. J. Modulation Doping via a 2D Atomic Crystalline Acceptor. *Nano Lett.* 2020. https://arxiv.org/abs/2007.06603 (accessed on July 13, 2020).
(12) Yu, Y.-J.; Zhao, Y.; Ryu, S.; Brus, L. E.; Kim, K. S.; Kim, P. Tuning the Graphene Work Function by Electric Field Effect. *Nano Lett.* **2009**, *9*, 3430−3434.
(13) Sears, J. A.; Songvilay, M.; Plumb, K. W.; Clancy, J. P.; Qiu, Y.; Zhao, Y.; Parshall, D.; Kim, Y.-J. Magnetic order in α-$RuCl_3$: A honeycomb-lattice quantum magnet with strong spin-orbit coupling. *Phys. Rev. B: Condens. Matter Mater. Phys.* **2015**, *91*, 144420.
(14) Plumb, K. W.; Clancy, J. P.; Sandilands, L. J.; Shankar, V. V.; Hu, Y. F.; Burch, K. S.; Kee, H.-Y.; Kim, Y.-J. α-$RuCl_3$: A spin-orbit assisted Mott insulator on a honeycomb lattice. *Phys. Rev. B: Condens. Matter Mater. Phys.* **2014**, *90*, 041112.
(15) Okamoto, S. Global phase diagram of a doped Kitaev-Heisenberg model. *Phys. Rev. B: Condens. Matter Mater. Phys.* **2013**, *87*, 064508.
(16) Wu, L.; Little, A.; Aldape, E. E.; Rees, D.; Thewalt, E.; Lampen-Kelley, P.; Banerjee, A.; Bridges, C. A.; Yan, J. Q.; Boone, D.; Patankar, S.; Goldhaber-Gordon, D.; Mandrus, D.; Nagler, S. E.; Altman, E.; Orenstein, J. Field evolution of magnons in α-$RuCl_3$ by high-resolution polarized terahertz spectroscopy. *Phys. Rev. B: Condens. Matter Mater. Phys.* **2018**, *98*, 094425.
(17) Banerjee, A.; Bridges, C. A.; Yan, J. Q.; Aczel, A. A.; Li, L.; Stone, M. B.; Granroth, G. E.; Lumsden, M. D.; Yiu, Y.; Knolle, J.; Bhattacharjee, S.; Kovrizhin, D. L.; Moessner, R.; Tennant, D. A.; Mandrus, D. G.; Nagler, S. E. Proximate Kitaev quantum spin liquid behaviour in a honeycomb magnet. *Nat. Mater.* **2016**, *15*, 733−740.
(18) Gerber, E.; Yao, Y.; Arias, T. A.; Kim, E.-A. Ab Initio Mismatched Interface Theory of Graphene on α- RuCl 3: Doping and Magnetism. *Phys. Rev. Lett.* **2020**, *124*, 106804.
(19) Wen, F.; Zhang, Y.; Gottheim, S.; King, N. S.; Zhang, Y.; Nordlander, P.; Halas, N. J. Charge Transfer Plasmons: Optical Frequency Conductances and Tunable Infrared Resonances. *ACS Nano* **2015**, *9*, 6428−6435.
(20) Ni, G. X.; McLeod, A. S.; Sun, Z.; Wang, L.; Xiong, L.; Post, K. W.; Sunku, S. S.; Jiang, B. Y.; Hone, J.; Dean, C. R.; Fogler, M. M.; Basov, D. N. Fundamental limits to graphene plasmonics. *Nature* **2018**, *557*, 530−533.
(21) Woessner, A.; Lundeberg, M. B.; Gao, Y.; Principi, A.; Alonso-González, P.; Carrega, M.; Watanabe, K.; Taniguchi, T.; Vignale, G.; Polini, M.; Hone, J.; Hillenbrand, R.; Koppens, F. H. L. Highly confined low-loss plasmons in graphene−boron nitride heterostructures. *Nat. Mater.* **2015**, *14*, 421−425.
(22) Naik, G. V.; Shalaev, V. M.; Boltasseva, A. Alternative Plasmonic Materials: Beyond Gold and Silver. *Adv. Mater.* **2013**, *25*, 3264−3294.
(23) Atkin, J. M.; Berweger, S.; Jones, A. C.; Raschke, M. B. Nano-optical imaging and spectroscopy of order, phases, and domains in complex solids. *Adv. Phys.* **2012**, *61*, 745−842.
(24) Luo, X.; Qiu, T.; Lu, W.; Ni, Z. Plasmons in graphene: recent progress and applications. *Mater. Sci. Eng., R* **2013**, *74*, 351−376.
(25) Bosman, M.; Ye, E.; Tan, S. F.; Nijhuis, C. A.; Yang, J. K. W.; Marty, R.; Mlayah, A.; Arbouet, A.; Girard, C.; Han, M.-Y. Surface plasmon damping quantified with an electron nanoprobe. *Sci. Rep.* **2013**, *3*, 1312−1312.
(26) Dai, S.; Ma, Q.; Liu, M.; Andersen, T.; Fei, Z.; Goldflam, M.; Wagner, M.; Watanabe, K.; Taniguchi, T.; Thiemens, M.; Keilmann, F.; Janssen, G.; Zhu, S.-E.; Jarillo-Herrero, P.; Fogler, M.; Basov, D. Graphene on hexagonal boron nitride as a tunable hyperbolic metamaterial. *Nat. Nanotechnol.* **2015**, *10*, 682−686.
(27) Biswas, S.; Li, Y.; Winter, S. M.; Knolle, J.; Valentí, R. Electronic Properties of α-$RuCl_3$ in Proximity to Graphene. *Phys. Rev. Lett.* **2019**, *123*, 237201.
(28) Götze, W.; Wölfle, P. Homogeneous Dynamical Conductivity of Simple Metals. *Phys. Rev. B* **1972**, *6*, 1226−1238.
(29) Volkov, V.; Mikhailov, S. A. Edge magnetoplasmons: low frequency weakly damped excitations in inhomogeneous two-dimensional electron systems. *Sov. Phys. JETP* **1988**, *67*, 1639−1653.
(30) Fei, Z.; Goldflam, M. D.; Wu, J. S.; Dai, S.; Wagner, M.; McLeod, A. S.; Liu, M. K.; Post, K. W.; Zhu, S.; Janssen, G. C. A. M.; Fogler, M. M.; Basov, D. N. Edge and Surface Plasmons in Graphene Nanoribbons. *Nano Lett.* **2015**, *15*, 8271−8276.
(31) Nikitin, A. Y.; Alonso-González, P.; Vélez, S.; Mastel, S.; Centeno, A.; Pesquera, A.; Zurutuza, A.; Casanova, F.; Hueso, L. E.; Koppens, F. H. L.; Hillenbrand, R. Real-space mapping of tailored sheet and edge plasmons in graphene nanoresonators. *Nat. Photonics* **2016**, *10*, 239−243.
(32) Gonçalves, P. A. D.; Xiao, S.; Peres, N. M. R.; Mortensen, N. A. Hybridized Plasmons in 2D Nanoslits: From Graphene to Anisotropic 2D Materials. *ACS Photonics* **2017**, *4*, 3045−3054.
(33) Bader, R. F. W. Principle of stationary action and the definition of a proper open system. *Phys. Rev. B: Condens. Matter Mater. Phys.* **1994**, *49*, 13348−13356.
(34) Das, A.; Pisana, S.; Chakraborty, B.; Piscanec, S.; Saha, S. K.; Waghmare, U. V.; Novoselov, K. S.; Krishnamurthy, H. R.; Geim, A. K.; Ferrari, A. C.; Sood, A. K. Monitoring dopants by Raman scattering in an electrochemically top-gated graphene transistor. *Nat. Nanotechnol.* **2008**, *3*, 210−215.
(35) Alonso-González, P.; Nikitin, A. Y.; Gao, Y.; Woessner, A.; Lundeberg, M. B.; Principi, A.; Forcellini, N.; Yan, W.; Vélez, S.; Huber, A. J.; Watanabe, K.; Taniguchi, T.; Casanova, F.; Hueso, L. E.; Polini, M.; Hone, J.; Koppens, F. H. L.; Hillenbrand, R. Acoustic terahertz graphene plasmons revealed by photocurrent nanoscopy. *Nat. Nanotechnol.* **2017**, *12*, 31−35.
(36) Xiong, L.; Forsythe, C.; Jung, M.; McLeod, A. S.; Sunku, S. S.; Shao, Y. M.; Ni, G. X.; Sternbach, A. J.; Liu, S.; Edgar, J. H.; Mele, E. J.; Fogler, M. M.; Shvets, G.; Dean, C. R.; Basov, D. N. Photonic crystal for graphene plasmons. *Nat. Commun.* **2019**, *10*, 4780.
(37) Pizzocchero, F.; Gammelgaard, L.; Jessen, B. S.; Caridad, J. M.; Wang, L.; Hone, J.; Bøggild, P.; Booth, T. J. The hot pick-up technique for batch assembly of van der Waals heterostructures. *Nat. Commun.* **2016**, *7*, 11894.
(38) Purdie, D. G.; Pugno, N. M.; Taniguchi, T.; Watanabe, K.; Ferrari, A. C.; Lombardo, A. Cleaning interfaces in layered materials heterostructures. *Nat. Commun.* **2018**, *9*, 5387.
(39) Kresse, G.; Furthmüller, J. Efficient iterative schemes for ab initio total-energy calculations using a plane-wave basis set. *Phys. Rev. B: Condens. Matter Mater. Phys.* **1996**, *54*, 11169−11186.
(40) Perdew, J. P.; Burke, K.; Ernzerhof, M. Generalized gradient approximation made simple. *Phys. Rev. Lett.* **1996**, *77*, 3865.

https://dx.doi.org/10.1021/acs.nanolett.0c03466
Nano Lett. XXXX, XXX, XXX−XXX

Supporting Information

Charge-Transfer Plasmon Polaritons at Graphene/α-$RuCl_3$ Interfaces

Daniel J. Rizzo[1], Bjarke S. Jessen[1,2], Zhiyuan Sun[1], Francesco L. Ruta[1,3], Jin Zhang[4], Jia-Qiang Yan[5,6], Lede Xian[4], Alexander S. McLeod[1], Michael E. Berkowitz[1], Kenji Watanabe[7], Takashi Taniguchi[8], Stephen E. Nagler[9], David G. Mandrus[5,6], Angel Rubio[4,10,11], Michael M. Fogler[12], Andrew J. Millis[1,10], James C. Hone[2], Cory R. Dean[1], D.N. Basov[1,*]

[1]Department of Physics, Columbia University, New York, New York 10027, United States

[2]Department of Mechanical Engineering, Columbia University, New York, New York 10027, United States

[3]Department of Applied Physics and Applied Mathematics, Columbia University, New York, New York 10027, United States

[4]Theory Department, Max Planck Institute for Structure and Dynamics of Matter and Center for Free-Electron Laser Science, 22761 Hamburg, Germany

[5]Materials Science and Technology Division, Oak Ridge National Laboratory, Oak Ridge, Tennessee 37831, United States

[6]Department of Materials Science and Engineering, University of Tennessee, Knoxville, Tennessee 37996, United States

[7]Research Center for Functional Materials, National Institute for Materials Science, 1-1 Namiki, Tsukuba 305-0044, Japan

[8]International Center for Materials Nanoarchitectonics, National Institute for Materials Science, 1-1 Namiki, Tsukuba 305-004, Japan

[9]Neutron Scattering Division, Oak Ridge National Laboratory, Oak Ridge, Tennessee 37831, United States

[10]Center for Computational Quantum Physics, Flatiron Institute, New York, New York 10010, United States

[11]Nano-Bio Spectroscopy Group, Universidad del País Vasco UPV/EHU, San Sebastián 20018, Spain

[12]Department of Physics, University of California San Diego, La Jolla, California 92093, United States

*Email: db3056@columbia.edu .

Table of Contents

Supplementary Discussion

S1. Fitting Calculated Plasmon Dispersions to the Experimental Data

I. *Modeling the surface and edge CPP dispersions*

In this section we discuss our analytical formalism for modeling the CPP excitations in our experimental device. The system geometry adopted in the model is shown schematically in Figure S8. We treated graphene as a 2D Drude metal of negligible thickness and sheet conductivity

$$\sigma_g(\omega) = \frac{i}{\pi}\frac{D_g}{\omega + i\gamma_g(\omega)}, \tag{S1}$$

where γ_g is the frequency-dependent damping rate discussed in the main text and section S2 and $D_g = (e^2/\hbar^2)|\mu|$ is the Drude weight proportional to the graphene chemical potential μ. The carrier density in graphene satisfies the equation $|n| = (|\mu|/\hbar v_F)^2/\pi$, where $v_F = 10^8 \text{cm s}^{-1}$ is the graphene Fermi velocity. We refer to the *h*BN layer above the graphene plus the vacuum beyond it as the graphene superstrate. We refer to the stack of layers below graphene as the graphene substrate. In our model, the substrate consists of a doped α-$RuCl_3$ layer, an undoped α-$RuCl_3$, and an SiO_2 layer.

We indexed all the layers in the super- and substrate consecutively from top to bottom by integer $j = 0, \ldots, 4$ and denoted their thicknesses by d_j. Thicknesses d_0 and d_4 are set to be infinite. The numerical values of *h*BN thickness $d_1 = 2.9$ nm and the total α-$RuCl_3$ thickness $d_2 + d_3 = 2.5$ nm were inferred from atomic force microscopy (AFM). The discontinuous change in doping of α-$RuCl_3$ is a simplifying assumption; in fact, the doping level should vary gradually. To model the doping of only the interfacial layers as suggested by the DFT, we set $d_3 = 1.9$ nm. In the first approximation, the doped α-$RuCl_3$ layer and graphene act as a single 2D system with a certain total sheet conductivity $\sigma = \sigma_g + \sigma_s$.

To take advantage of the approach developed in a previous work[1] and also for greater generality, we modeled each layer as a uniaxial dielectric with an in-plane permittivity $\epsilon_j^{\perp}(\omega)$ and an out-of-plane permittivity $\epsilon_j^{\parallel}(\omega)$. The geometric average of these quantities is denoted by $\epsilon_j \equiv \left(\epsilon_j^{\perp}\right)^{1/2}\left(\epsilon_j^{\parallel}\right)^{1/2}$. In the actual calculation, only the *h*BN layer was treated as uniaxial. The permittivity of all the other layers was taken to be isotropic, $\epsilon_j^{\perp} = \epsilon_j^{\parallel} = \epsilon_j$. This simplifying assumption may be a source of some inaccuracy because α-$RuCl_3$ is monoclinic at room temperature. Finally, we described the effect of doping on α-$RuCl_3$ by another phenomenological correction of Drude type:

$$\epsilon_2^a(\omega) - \epsilon_3^a(\omega) = -\frac{(\nu^a)^2}{\omega(\omega + i\gamma_s)}, \qquad a = \perp \text{ or } z, \tag{S3}$$

where ν^a and γ_s are adjustable parameters. As mentioned above, if d_2 is small, it is permissible to lump layer 2 with graphene by converting the in-plane correction $\epsilon_2^{\perp}(\omega) - \epsilon_3^{\perp}(\omega)$ into the correction to graphene sheet conductivity:

$$\sigma_s(\omega) = \frac{i}{\pi}\frac{D_s}{\omega + i\gamma_s(\omega)}, \qquad D_s = \frac{1}{4}(\nu^{\perp})^2 d_2 . \tag{S4}$$

(Conversely, if σ_s and d_2 are considered primary parameters, one can use these equations to obtain $\epsilon_2^{\perp} - \epsilon_3^{\perp}$). Assuming the 2D carrier density in the doped α-$RuCl_3$ layer is equal in magnitude and opposite in sign to that in graphene, we can estimate the corresponding 2D Drude weight by $D_s =$

$\pi|n|e^2/m^*$ where the lower bound of the effective mass of carriers m^* is provided by the DFT. The scattering rate $\gamma_s(\omega)$ is discussed in more detail in Section S2 below.

The influence of the substrate and the superstrate on electrodynamics of charge carriers in graphene can be described by frequency and momentum dependent permittivities, $\kappa_{\rm sub} = \kappa_{\rm sub}(\omega, q)$ and $\kappa_{\rm sup} = \kappa_{\rm sup}(\omega, q)$. In the quasi-static limit $q \gg \omega/c$, which is relevant for our near-field experiment, we can compute these quantities from the formula

$$\kappa_{\rm s} = (1 + r_{Ps})/(1 - r_{Ps}) \ , \quad s = \text{sub or sup.} \tag{S5}$$

This equation derives from the quasi-static approximation for the P-polarization Fresnel reflection coefficient of $j,\ j+1$ interface: $r_{j,j+1} \simeq \big(\epsilon_{j+1} - \epsilon_j\big)/\big(\epsilon_{j+1} + \epsilon_j\big)$. Specifically, Eq. (S5) can be derived once the replacements $r_{j,j+1} \to r_{Ps}$, $\epsilon_{j+1} \to \kappa_s$, and $\epsilon_j \to \epsilon_0 = 1$ are made. Here r_{Ps} is the reflection coefficient of the stack s. To compute such r_{Ps} we used the recursion method of [1]. For the case of substrate, it is applied as follows. The base of the recursion is a partial reflection coefficient $r_{M-1} \equiv r_{M-1,M}$ where $M = 4$ is the index of the bottom substrate layer, i.e., the layer farthest from graphene. At each recursion step, another partial reflection coefficient r_j is computed, for j lowered by one, (that is, for one position closer to graphene). The net reflection coefficient $r_{P\,\rm sub}$ is given by $r_{P\,\rm sub} = r_N$ where $N = 1$ is the index of the substrate layer next to graphene. In the cited reference [1], a more general model was considered where interfaces between adjacent layers $j,\ j+1$ were assumed to have some sheet conductivities $\sigma_{j,j+1}$, in which case the full set of equations employed in the calculation is

$$\begin{aligned} r_j &= r_{j,j+1} - \frac{\big(1 - r_{j,j+1}\big)\big(1 - r_{j+1,j}\big)r_{j+1}}{r_{j+1,j}\, r_{j+1} - \exp\big(-2ik^z_{j+1}d_{j+1}\big)} \ , \\ r_{j,j+1} &= \frac{Q_{j+1} - Q_j + \dfrac{4\pi}{\omega}\sigma_{j,j+1}}{Q_{j+1} + Q_j + \dfrac{4\pi}{\omega}\sigma_{j,j+1}} \ , \\ Q_j &= \frac{\epsilon^\perp_j}{k^z_j} \ , \quad k^z_j = \sqrt{\epsilon^\perp_j}\sqrt{\frac{\omega^2}{c^2} - \frac{q^2}{\epsilon^\parallel_j}} \ . \end{aligned} \tag{S6}$$

In the generic case $d_2 > 0$, only $\sigma_{12} = \sigma_g$ is nonzero and actually it does not enter the calculation of $r_{P\,\rm sub}$ because the recursion terminates at $j = 1$. However, by continuing through to $j = 0$, we can obtain the reflection coefficient r_P of the entire heterostructure (the top encapsulating layer plus graphene plus the substrate stack). To compute the refection coefficient $r_{P\,\rm sup}$ of the superstrate, we followed the same scheme as for $r_{P\,\rm sub}$ except with the layer order inverted, i.e., we always run the recursion from the layer farthest from graphene to the one closest to it. It is easy to derive a closed-form expression for $\kappa_{\rm sup}$:

$$\kappa_{\rm sup} = \epsilon_1 \frac{\epsilon_0 + \epsilon_1 \tanh(-ik^\parallel_1 d_1)}{\epsilon_1 + \epsilon_0 \tanh(-ik^\parallel_1 d_1)} \ , \quad k^\parallel_1 = i\frac{\sqrt{\epsilon^\perp_1}}{\sqrt{\epsilon^\parallel_1}}q \ . \tag{S7}$$

The net effective permittivity of the graphene environment is equal to the average of the substrate and superstrate permittivities:

$$\kappa(\omega, q) = (\kappa_{\rm sub} + \kappa_{\rm sup})/2 = \kappa_1 + i\kappa_2 \ . \tag{S8}$$

The momentum dependence of function $\kappa(\omega, q)$ can be understood from the following qualitative argument. The electric field created by charges in graphene spreads over the vertical

distance that scales as $1/q$. Therefore, at large q, the field is strongly confined in the layers $j = 1$ and $j = 2$ adjacent to graphene, so that κ should approach the average of their permittivities:

$$\kappa(\omega, \infty) = (\epsilon_1 + \epsilon_2)/2\,. \tag{S9}$$

Conversely, at small q, the electric field penetrates far beyond the adjacent layers and resides mainly in the semi-infinite $j = 0$ and $j = 4$ strata (vacuum and SiO_2), so that $\kappa \approx (\epsilon_0 + \epsilon_4)/2$. At intermediate momenta, the function κ should smoothly interpolate between these limiting values.

Once κ is known, we can compute the effective 2D dielectric function of graphene. It has a well-known form

$$\epsilon(\omega, q) = 1 - \frac{1}{\kappa(\omega, q)}\frac{q}{q_p(\omega)}, \qquad q_p(\omega) \equiv \frac{i\omega}{2\pi\sigma_g(\omega)} = \frac{\omega(\omega + i\gamma)}{2D_g}, \tag{S10}$$

where $q_p(\omega)$ has the physical meaning of the CPP momentum of graphene suspended in vacuum, $\kappa = 1$.

To handle $d_2 \to 0$ limit, it is natural to introduce two obvious changes into this general scheme. The first one is to replace σ_g in Eq. (S10) by $\sigma_g + \sigma_s$. The second one is to redefine the substrate as layers $j = 3$ plus 4 only. The corresponding κ_{sub} is given by [cf. Eq. (S7)]

$$\kappa_{\text{sub}} = \epsilon_3 \frac{\epsilon_4 + \epsilon_3 \tanh(-ik_3^{\parallel} d_3)}{\epsilon_3 + \epsilon_4 \tanh(-ik_3^{\parallel} d_3)}, \quad k_3^{\parallel} = i\frac{\sqrt{\epsilon_3^{\perp}}}{\sqrt{\epsilon_3^{\parallel}}} q\,. \tag{S11}$$

In this reformulation, $\kappa_{\text{sub}} \to \epsilon_3$ as $q \to \infty$.

To compute the dispersions of the CPPs and edge CPPs we analyzed the behavior of the dielectric function $\epsilon(\omega, q)$. For the CPP, our procedure was as follows. The complex CPP momentum $q_s = q_1 + iq_2$ is the root of $\epsilon(\omega, q)$ for a given real ω, which, per Eq. (S9), is the solution of the equation

$$q_s = q_p(\omega)\kappa(\omega, q)\,. \tag{S10}$$

To find the real part $q_1 = \text{Re}\, q_s$ of this solution we employed an approximation that $q_1(\omega)$ coincides with the maximum of the loss function of graphene

$$f(\omega, q) \equiv -\text{Im}\frac{1}{\epsilon(\omega, q)}. \tag{S11}$$

This approximation is justified for the experimentally relevant case of weakly damped CPP, $q_2 \ll q_1$. Once q_1 is determined, we can get q_2 using Eq. (1) of the main text:

$$Q^{-1} = \frac{q_2}{q_1} \simeq \frac{\kappa_2(\omega, q_1)}{\kappa_1(\omega, q_1)} + \frac{\text{Im}\, q_p}{\text{Re}\, q_p} = \frac{\kappa_2(\omega, q_1)}{\kappa_1(\omega, q_1)} + \frac{\gamma}{\omega}. \tag{S12}$$

This perturbative result follows from Eq. (S10) and is valid assuming both terms on the right-hand side are small.

We also implemented another method for determining the CPP dispersion, which is to look for the maxima of the imaginary part of the total reflection coefficient $r_P(\omega, q)$. For the simple case where the encapsulating layer $j = 1$ is absent, so that $\kappa_{\text{sup}} = \epsilon_0$, the equivalence of the two methods can be seen from the formula $r_P = 1 - 2\kappa_{\text{sub}}(\kappa_{\text{sub}} + \epsilon_0)^{-1}\epsilon^{-1}$ [which follows from Eq. (S6)], implying that a sharp maximum of $f(\omega, q)$ is also a maximum of $\text{Im}\, r_P$. Note that the imaginary parts of κ, ϵ, and r_P are all positive if ω and $q > \omega/c$ are real. We verified numerically that in the frequency range of interest, these two methods, both very common, give virtually the

same results. Our calculations were done using fminbnd function of Matlab[2]. The results are shown in two figures of the main text: Figure 2c (where the false color background represents Im r_P) and Figure 4b (where the dashed lines are the ridges of the loss function f). Additionally, the results obtained for the $d_2 \to 0$ limit are shown in Figures S6 and S7. These results are discussed in more detail in Section S1 II below.

The perturbative analysis can also be applied if the doped α-$RuCl_3$ layer has a sufficiently small thickness and the corresponding sheet conductivity σ_s is a relatively small correction to the graphene conductivity σ_g. Using Eq. (S9) and (S10), we can obtain the first-order shift δq of the CPP momentum due to σ_s or vice versa, σ_s as a function of δq:

$$\frac{\sigma_s}{\sigma} \approx \frac{\delta q}{q}\left(1 - \frac{q_p}{\kappa}\frac{\partial \kappa}{\partial q_p}\right). \tag{S13}$$

Let us now turn to the edge CPP. In calculating their dispersion, we relied on the analytical theory presented in Ref. [3]. This theory predicts that the edge excitations show up as the poles of a certain function $g(\omega, q)$ defined by

$$g(\omega, q) = \tanh I\,, \qquad I = \frac{1}{\pi}\int_0^{\pi} \frac{d\xi}{1+\xi^2} \ln \epsilon\left(\sqrt{1+\xi^2}\, q, \omega\right). \tag{S14}$$

This function seems to be a one-dimensional analog of the response functions f and r_P we used to analyze the CPP. However, according to our numerical simulations, neither real nor imaginary part of g has a definite sign, unlike Ref or Im r_P. Therefore, we adopted the prescription that the real part of the edge CPP momentum q_e coincides with the maximum of the *absolute value* of $g(\omega, q)$. To find such a maximum, we used the same Matlab function as before. The results are shown in Figure 4b of the main text (solid lines).

For a qualitative understanding of the computed edge CPP spectra, two analytical results are useful. First, as explained above, the effective permittivity κ approaches constant values in the limit of both small and large q. In this limit, the edge and CPP momenta are connected by a simple rule: the former is $A = 1.217$ times larger than the latter[3]. This "universal" relation can be derived by noticing that the poles of g correspond to $I = i\pi/2$, which entails an alternative form of the edge CPP dispersion equation (obtained after the substitution $\xi = q\cot t$):

$$\int_0^{\pi/2} dt \ln\left[-\epsilon\left(\frac{q_e}{\sin t}, \omega\right)\right] = \int_0^{\pi/2} dt \ln\left[\frac{k}{q_p(\omega)\kappa(\omega, k)} - 1\right]\Bigg|_{k=\frac{q_e}{\sin t}} = 0\,. \tag{S15}$$

If κ is momentum-independent, this equation is easy to solve numerically to obtain the quoted result $q_e = Aq_s$. However, in our case κ is not constant, primarily because of the presence of the *h*BN overlayer. As a result, the edge-to-surface CPP momentum ratio for the computed dispersions is typically larger than 1.217, sometimes as high as 1.6 (see Figure 4b). The fact that a few-nm thick layer of *h*BN has such a strong effect on edge CPPs indicates that the edge CPP has a substantial contribution of high-momenta Fourier harmonics whose electric field is confined inside *h*BN. The second analytical result concerns the 2D sheet model of the doped α-$RuCl_3$ layer. From a perturbative analysis of Eq. (S15) we obtained the following counterpart of Eq. (S13):

$$\frac{\sigma_s}{\sigma} \approx \frac{\delta q_e}{q_e}\left(1 - \overline{\frac{q_p}{\kappa}\frac{\partial \kappa}{\partial q_p}}\right),$$
$$\overline{z(q)} \equiv \frac{\int_q^\infty w(q,k) z(k) dk}{\int_q^\infty w(q,k) dk}, \tag{S16}$$
$$w(q,k) = \frac{1}{\sqrt{k^2 - q^2}} \frac{1}{k - \kappa q_p}.$$

In words, the coefficient for the fractional shift of the edge CPP momentum is given by the average of the logarithmic derivative of κ, weighted with the function $w(q,k)$. This weighting function can be thought of as the relative contribution of different Fourier harmonics to the total real-space waveform of the edge CPP excitation.

In the next Section we discuss numerical simulations and fits based on the equations presented in this Section.

II. *Least-squares optimization of the chemical potential*

Since the magnitude of charge transfer between the graphene and α-$RuCl_3$ layers was unknown, the chemical potential of graphene was made a free parameter in a least-squares fit to the measured CPP dispersions. The objective function χ^2 to minimize is the residual squared difference between experimental and model plasmon momenta weighted by the observation uncertainties:

$$\chi^2 = \sum_{i=1}^{N_\omega} \frac{\left(q_{s,i} - q_{\mathrm{s,i}}^{obs}\right)^2}{\sigma_{obs,i}^2} \tag{S17}$$

where q_{s}^{obs} and σ_{obs}^2 are, respectively, the mean and variance of the observed plasmon momenta, and N_ω is the number of experiments at different laser frequencies. The fitting was done assuming $d_2 \to 0$ limit ($d_3 = 1.9\, nm$), with κ computed from Eqs. (S7), (S8), and (S11). When the conductivity of the doped α-$RuCl_3$ layer, Eq. (S4), was included in the calculations with the effective mass equal to the vacuum free electron mass, a value of $|\mu| = 0.56^{+0.02}_{-0.04}$ eV minimized the residual, see Figure S5. We also considered a scenario where this effective mass was infinitely heavy so that the doping-induced modification of the permittivity of α-$RuCl_3$ was absent, $\epsilon_2 - \epsilon_3 = 0$ and $d_3 = 2.5\, nm$. We found that in this case the best fit was $|\mu| = 0.62^{+0.03}_{-0.03}$ eV, but agreement between the calculated upper polariton branch and the data appeared worse for our choice of parameters, cf. Figures S5a and S5b. The error bars are likelihood-based confidence intervals[4] describing the parameter space within thresholds on the residual. Thresholds are computed by the quantile function of a chi-squared distribution with a 95% confidence level and 40 degrees of freedom, i.e. the various inputs of the near-field model.[5]

For numerical values of the *h*BN and SiO_2 permittivities needed in the calculations, we used the following analytical parametrizations. The in- and out-of-plane responses of *h*BN were modeled with a single-oscillator Drude-Lorentz forms

$$\epsilon^a(\omega) = \epsilon_\infty^a + \epsilon_\infty^a \frac{(\omega_{LO}^a)^2 - (\omega_{\mathrm{TO}}^a)^2}{(\omega_{\mathrm{TO}}^a)^2 - \omega^2 - i\gamma^a \omega} \tag{S18}$$

The permittivity of SiO_2, which is isotropic, was modeled as the sum of multiple Lorentzians:

$$\epsilon(\omega) = \epsilon_\infty + \sum_i \frac{\Omega_i^2}{\omega_i^2 - \omega^2 - i\gamma_i\omega}. \quad \text{(S19)}$$

The permittivity of undoped α-$RuCl_3$ was taken from Ref. [6]. As mentioned in Section S1 I, we treated it as isotropic as well. We fitted this permittivity to the sum of three Lorentzians with parameters given in Table S1. The parameters for *h*BN and SiO_2 were taken from Refs. [7,8]. The parameters are summarized in Tables S2 and S3. We then fitted the CPP dispersions using the chemical potential μ of graphene as the adjustable parameter, as described above.

i	ω_i ($\mathrm{cm^{-1}}$)	Ω_i ($\mathrm{cm^{-1}}$)	γ_i ($\mathrm{cm^{-1}}$)
1	753.9	2222	941.7
2	276.7	2555	470.7
3	378.4	190.7	101.0

Table S1: Oscillator parameters for α-$RuCl_3$ for use in the frequency range $750 < \omega(\mathrm{cm^{-1}}) < 2500$. The high-frequency permittivity is $\epsilon_\infty = 6.191$[6].

	ω_{TO} ($\mathrm{cm^{-1}}$)	ω_{LO} ($\mathrm{cm^{-1}}$)	γ ($\mathrm{cm^{-1}}$)	ϵ_∞
$\epsilon^\perp$	1360	1614	7	4.9
$\epsilon^\parallel$	760	825	2	2.95

Table S2: Oscillator parameters for *h*BN[7] **.**

i	ω_i ($\mathrm{cm^{-1}}$)	Ω_i ($\mathrm{cm^{-1}}$)	γ_i ($\mathrm{cm^{-1}}$)
1	1172	282.8	13
2	1090	538.5	12
3	1060	529.2	5
4	803	200.0	35
5	460	382.1	13
6	544	289.8	164

Table S3: Oscillator parameters for SiO_2. The high-frequency permittivity is $\epsilon_\infty = 1.96$ [8].

In summary, fitting the CPP dispersions, i.e., q_1, to the data alone is indicative but probably not sufficient for verifying the existence of a modified optical response from charge transfer into interfacial α-$RuCl_3$ layers. However, further stronger evidence for the doping of α-$RuCl_3$ is found from analyzing q_2 and deduced from the plasmon quality factor Q, as discussed in Section S2 below.

S2. Characterizing the graphene/α-$RuCl_3$ interfacial optical response from the CPP losses

I. *Graphene phonon contribution to the plasmon scattering rate*

As shown in Ref. [9], in clean graphene such as exfoliated samples encapsulated in *h*BN, electron-phonon scattering is the major contributions to the CPP damping. The relevant phonons are the two acoustic phonons [transverse (TA) and longitudinal (LA)], the A_1' optical phonon around *K* point and the two optical phonons around Γ point (TO and LO, degenerate at Γ). Below we summarize the main steps of the calculation presented in Ref. [9]. The starting point is the formula $P = 2\sigma_1(\omega)|E|^2$ for the power dissipation in the presence of an oscillating electric field $E\ e^{-i\omega t} + \text{c. c.}$ It implies that the scattering rate can be computed as

$$\gamma(\omega) = \omega\frac{\sigma_1}{\sigma_2} = \frac{\pi}{2}\frac{\omega^2}{D_g}\frac{P}{|E|^2} \tag{S20}$$

assuming $\gamma \ll \omega$. The power dissipation can be found from the Fermi's golden rule[9]:

$$\begin{aligned} P = 2\pi\omega\left|\frac{eE}{\omega}\right|^2 \int \frac{Nd^2k}{(2\pi)^2}\frac{d^2k}{(2\pi)^2}\sum_{\zeta,\zeta_\gamma}\sum_{S,S'}\sum_{v=l,t}\zeta\zeta_\gamma f(\varepsilon_{S\boldsymbol{k}})[1-f(\varepsilon_{S'\boldsymbol{k}'})] \\ \times\left[n_B\left(\zeta\hbar\omega_{v\boldsymbol{q}}\right)+1\right]\delta\left(\varepsilon_{S'\boldsymbol{k}'}-\varepsilon_{S\boldsymbol{k}}+\zeta\hbar\omega_{v\boldsymbol{q}}-\zeta_\gamma\hbar\omega\right) \\ \times\left|\sum_{S''}\frac{W^v_{S'\boldsymbol{k}';S''\boldsymbol{k}}v^x_{S''\boldsymbol{k};S\boldsymbol{k}}}{\varepsilon_{S\boldsymbol{k}}-\varepsilon_{S''\boldsymbol{k}}+\zeta_\gamma\hbar\omega}-\frac{v^x_{S'\boldsymbol{k}';S''\boldsymbol{k}'}W^v_{S''\boldsymbol{k}';S\boldsymbol{k}}}{\varepsilon_{S'\boldsymbol{k}'}-\varepsilon_{S''\boldsymbol{k}'}+\zeta_\gamma\hbar\omega}\right|^2 \end{aligned} \tag{S21}$$

where $W^v_{S'\boldsymbol{k}';S\boldsymbol{k}}$ is the electron-phonon couple matrix element between the states (*S'*, *k'*) and (*S*, *k*), $f(\varepsilon)$ is the Fermi occupation number at energy ε and n_B is the phonon occupation number. The transition matrix element due to LA/TA phonons is

$$W^v = i\beta_A\sqrt{\frac{\hbar q^2}{\mu_S\omega_{vq}}}\begin{pmatrix}0 & i\\ -i & 0\end{pmatrix} \tag{S22}$$

in the pseudospin basis. It induces the scattering rate

$$\gamma_A(\omega) = \left(1+\frac{1}{12}\frac{\omega^2}{\mu^2}\right)\gamma(0) = \left(1+\frac{1}{12}\frac{\omega^2}{\mu^2}\right)\frac{1}{\hbar^3}\frac{\beta_A^2|\mu|}{\mu_S v_F^2}\left(\frac{1}{v_l^2}+\frac{1}{v_t^2}\right)T \tag{S23}$$

In deriving this formula, we assumed ω/μ is a small parameter and kept terms up to the order $O(\omega^2/\mu^2)$. The electron-phonon coupling constant $\beta_A = 5.0\ eV$ can be found in Refs. [9] or [10]. The lattice mass density is $\mu_s = 7.6\times10^{-8} g/cm^2$ and the phonon velocities are $v_l = 2.2\times10^6\ cm/s$, $v_t = 1.4\times10^6\ cm/s$. Equation (S22) indicates that the frequency dependence of γ_A is weak as long as $\omega < \mu$.

The transition matrix elements for the A_1' phonon is

$$W^K = i\beta_K\sqrt{\frac{2\hbar}{\mu_S\omega_K}}\begin{pmatrix}0 & i\\ -i & 0\end{pmatrix}, \tag{S24}$$

where $\beta_K = 14\ eV/\text{Å}$ and $\omega_K = 1200\ cm^{-1}$. The dominant process is the intra-band emission of the optical phonons. The corresponding scattering rate is

$$\begin{aligned} \gamma_K(\omega) = \frac{3}{2}\frac{\beta_K^2\mu^2}{\mu_S\omega_K\omega v_F^2}\sum_{\zeta,\zeta_\gamma}\zeta\zeta_\gamma\int_0^\infty dx x\left(x-\zeta\frac{\omega_K}{\mu}+\zeta_\gamma\frac{\omega}{\mu}\right)f(\mu x) \\ \times\left[1-f\left(\mu x-\zeta\omega_K+\zeta_\gamma\omega\right)\right][1+n_B(\zeta\omega_K)] \end{aligned} \tag{S25}$$

where ζ, ζ_γ take values of ±1. At zero temperature, considering photon (not phonon!) absorption only, this expression simplifies to

$$\begin{aligned}\gamma_K(\omega) &= \frac{3}{2}\frac{\beta_K^2\mu^2}{\mu_S\omega_K\omega v_F^2}\Theta(\omega-\omega_K)\int_{1-\frac{\omega-\omega_K}{\mu}}^{1} dx x\left(x+\frac{\omega-\omega_K}{\mu}\right) \\ &= \frac{3}{2}\frac{\beta_K^2\mu}{\mu_S\omega_K v_F^2}\Theta(\omega-\omega_K)\frac{\mu}{\omega}\left[\frac{\omega-\omega_K}{\mu}-\frac{1}{6}\left(\frac{\omega-\omega_K}{\mu}\right)^3\right]\end{aligned} \tag{S26}$$

Next, the combined scattering of TO and LO phonons results in an isotropic matrix element proportional to β_Γ. The intraband emissions of the TO/LO optical phonons contribute to the scattering rate and are the same as Eq. (S25) but with $\frac{3}{2} \to 1$ and β_K, ω_K replaced by $\beta_\Gamma = 11.4\ \mathrm{eV/Å}, \omega_\Gamma = 1600\ cm^{-1}$. At zero temperature, it simplifies to Eq. (S26), with the same replacement. Altogether, the phonon contribution to the scattering rate of graphene is

$$\gamma_g(\omega) = \gamma_A(\omega) + \gamma_K(\omega) + \gamma_\Gamma(\omega)\,. \tag{S27}$$

The values of the coupling constants can be found in Refs. [9] or [10].

II. *Extracted optical conductivity of doped α-RuCl₃*

To simplify the analysis, we again treat the doped part of α-$RuCl_3$ as two-dimensional, $d_2 \to 0$. In this case the scattering rate γ_{eff} is used in place of γ in Eq. (S12), and should be defined in terms of the total sheet conductivity $\sigma = \sigma_g + \sigma_s$. Its relation to the CPP Q factor $Q = q_1/q_2$ is as follows:

$$\gamma_{\mathrm{eff}}(\omega) \equiv \omega\,\frac{\mathrm{Re}\,\sigma(\omega)}{\mathrm{Im}\,\sigma(\omega)} = \omega\left[\frac{1}{Q}-\frac{\kappa_2(\omega,q_1)}{\kappa_1(\omega,q_1)}\right], \tag{S28}$$

where $\kappa = \kappa_1 + i\kappa_2$ is to be computed from Eqs. (S7), (S8), and (S11). After subtracting the contribution from the substrate, the measured effective frequency dependent scattering rate, γ_{eff}, is shown in Figures 4b and S9. If both graphene and α-$RuCl_3$ are described by Drude models with frequency dependent scattering rates, Eqs. (S1) and (S4) then become

$$\sigma(\omega) = \frac{i}{\pi}\frac{D_g}{\omega+i\gamma_g(\omega)} + \frac{i}{\pi}\frac{D_s}{\omega+i\gamma_s(\omega)}, \tag{S29}$$

and the effective scattering rate becomes

$$\gamma_{\mathrm{eff}}(\omega) \approx \frac{D_g}{D_g+D_s}\frac{\omega^2\gamma_g(\omega)}{\omega^2+\gamma_g^2(\omega)} + \frac{D_s}{D_g+D_s}\frac{\omega^2\gamma_s(\omega)}{\omega^2+\gamma_s^2(\omega)} \tag{S30}$$

From Eq. (S10), given the measured plasmon dispersion and damping, the optical conductivity of α-$RuCl_3$ can be extracted as

$$\sigma_s(\omega) = i\kappa(\omega,q)\frac{\omega}{2\pi q} - \sigma_g(\omega) \tag{S31}$$

Note that $q = q_1 + iq_2$ is the complex plasmon momentum while ω is a real number. It appears that the major effect of the doped α-$RuCl_3$ layer is to bring extra damping to the CPP rather than to shift their dispersion. Thus, the estimation of γ_g from Eq. (S27) shows that more than half of the total measured CPP losses can be due to the proximity to α-$RuCl_3$. As can be seen from

Figure 4c, a typical magnitude of the real part of optical conductivity is $\mathrm{Re}\,\sigma_s \approx 0.5\,e^2/h \approx 0.08\,e^2/\hbar$. We estimate the relative uncertainty of the extracted $\mathrm{Re}\,\sigma_s$ to be about 20%. However, it may contain a systematic error if our estimate of κ or the theoretical scattering rate in graphene is inaccurate, see Sec. S1 II. Nevertheless, the extraction of $\mathrm{Re}\,\sigma_s$ is more reliable than the extraction of $\mathrm{Im}\,\sigma_s$ or the Drude weight D_s.

Provided the measurement frequencies are not in the Drude tail $\omega < \gamma_s$, which seems likely, having such a low $\mathrm{Re}\,\sigma_s$ implies that the mean free path of carriers in α-$RuCl_3$ is much smaller than the interparticle distance. Given the interlayer distance[11] c = 0.57 nm, the upper bound on the equivalent bulk conductivity is $\mathrm{Re}\,\sigma_{3D} = \mathrm{Re}\,\sigma_s/c \approx 340\ (\Omega\,\mathrm{cm})^{-1}$. In comparison, a weakly-doped cuprate $La_{1.97}Sr_{0.03}CuO_4$ (LSCO) has a conductivity[12] of $200\ (\Omega\,\mathrm{cm})^{-1}$ in the in-plane direction. It corresponds to the 2D conductivity of $\sigma_{\mathrm{LSCO}} \approx 0.1\,e^2/\hbar$ per atomic layer considering the interlayer distance[13] of 1.32 nm.

Despite the shortness of the mean-free path, we can formally compare our findings for $\gamma_s(\omega)$ to the predictions of the Fermi liquid theory. The equation

$$\gamma_s(\omega) = [(k_B T)^2 + 0.18(\hbar\omega)^2]\ /\hbar E_F \tag{S32}$$

where $E_F = 63\ meV$ plugged into Eq. (S30) gives the blue curves in Figures S9 and 4a,b,f in the main text. From the comparison in Figure 4b of the main text, the experimental scattering rate $\gamma_s(\omega, T)$ of α-$RuCl_3$ increases with frequency faster than frequency squared. This is different from the behavior typically found in cuprates, where the scattering rate is linear in frequency and temperature.

S3. Modeling near-field signal from plasmon reflection at a point defect

We assumed that a defect in the graphene-α-$RuCl_3$ heterostructure caused a local perturbation of the total sheet conductivity $\sigma = \sigma_g + \sigma_s$ with respect to the asymptotic value $\sigma(\infty)$. We denote $\bar{\sigma}(\mathbf{r}) = \sigma(\mathbf{r})/\sigma(\infty)$ the corresponding relative change. To model the position-dependent near-field signal associated with reflections of CPP from the defect, we considered the integro-differential equation for the scalar potential ϕ_s generated in response to the potential ϕ_{probe} of a probe[14]:

$$\left[1 + \frac{1}{2\pi q_s} V * \nabla \cdot \bar{\sigma}(\mathbf{r})\, \nabla\right] \phi(\mathbf{r}) = \phi_{\mathrm{probe}}(\mathbf{r}), \quad \phi = \phi_{\mathrm{probe}} + \phi_s. \tag{S33}$$

Here q_s is the momentum of the CPP away from the defect [Eq. (S14)], $V(r) = 1/r$ is the Coulomb kernel, and the asterisk $(*)$ denotes the spatial convolution over the in-plane coordinate $\mathbf{r} = (x, y)$. As an example, we chose $\bar{\sigma}(\mathbf{r}) \equiv 1 + \delta\Lambda(r/w)$, where δ is the characteristic magnitude of the conductivity fluctuation at the defect, w is its width, and $\Lambda(z) = 1/(1+z^2)$ is a Lorentzian function of unit width and height. We solved Eq. (S33) through expansion in an orthonormal basis of plane waves $\phi_j = A_j e^{i\mathbf{q}_j \cdot \mathbf{r}}$ periodic in a 2D square cell $x, y \in [-L/2\,, L/2]$, with A_j a normalization constant. If we assemble the Fourier momenta $\mathbf{q}_j$ and the Fourier coefficients $\tilde{\phi}_j = \langle \phi_j | \phi \rangle \equiv \int \phi_j^*(\mathbf{r})\phi(\mathbf{r}) d^2 r$ into column vectors $\vec{q}$ and $\vec{\phi}$, respectively, these vectors must obey the equation

$$\vec{\phi} = \left[q_s - \left(\delta \overleftrightarrow{Q} + \mathrm{diag}\,|\vec{q}|\right)\right]^{-1} q_s \vec{\phi}_{\mathrm{probe}}\,, \tag{S34}$$

where $\overleftrightarrow{Q}$ is the scattering matrix with the elements

$$Q_{ij} = (\hat{\mathbf{q}}_i \cdot \mathbf{q}_j) \left\langle \phi_i \left| \Lambda\left(\frac{r}{w}\right) \right| \phi_j \right\rangle . \quad \text{(S35)}$$

We defined another matrix-valued function $\overleftrightarrow{G}$ by $\vec{\phi}_s = \overleftrightarrow{G}\, \vec{\phi}_{\text{probe}}$. From Eq. (S33), we obtain

$$G_{ij} = \left\langle \phi_i \middle| \left[q_0 - \left(\delta \overleftrightarrow{Q} + \text{diag}\,|\vec{q}|\right)\right]^{-1} \left(\delta \overleftrightarrow{Q} + \text{diag}\,|\vec{q}|\right) \middle| \phi_j \right\rangle. \quad \text{(S36)}$$

For translationally invariant system, $\delta = 0$, where the momentum is conserved, only the diagonal matrix elements are nonzero. They can be understood as "in-plane" reflection coefficients. The connection to the conventional Fresnel coefficients $r_P(\omega, q)$ and the graphene loss function $f(\omega, q)$ discussed in Section S1 is as follows: $-G_{jj} = 1 - \epsilon(\omega, \mathbf{q}_j)^{-1}$ where $\epsilon(\omega, \mathbf{q})$ is the effective dielectric function of graphene [Eq. (S9)]. Therefore, Im $(-G_{jj}) = f(\omega, \mathbf{q}_j)$ has maxima at the same momenta $|\mathbf{q}_j| = \text{Re}\, q_s$ as f and Im r_P. Previous theoretical work has shown that the Fresnel reflection coefficient $r_P(\omega, q_{\text{probe}})$ is representative of the near-field signal for homogeneous graphene. Here q_{probe} is of the order of the inverse curvature radius of the sharp tip of the probe. Motivated by this, we defined the generalized reflection coefficient associated with our spatially localized probe excitation,

$$R \equiv -\vec{\phi}_{\text{probe}}^{\,T} \overleftrightarrow{G}\, \vec{\phi}_{\text{probe}} . \quad \text{(S37)}$$

We expect that R should be representative of the local near-field signal produced by a general inhomogeneous system.

We developed a Python-language computer code implementing the above equations taking advantage of public-domain libraries and we used it to carry out a series of numerical simulations. For simplicity, we approximated $\phi_{\text{probe}}(\mathbf{r})$ by a potential of a point dipole placed a small distance away from graphene[15]. Given an in-plane probe position $\mathbf{r}_{\text{probe}}$, the relative strength δ of the perturbation due to the defect, and the defect width w, the code computes the absolute value of R. We varied parameters δ and w to achieve maps of $|R(\mathbf{r}_{\text{probe}})|$ resembling our experimental data. The results are presented in Figure 3 of the main text. Our simulations are consistent with the defect width of $w \sim 40$ nm, which is comparable to what was found in the AFM topography studies. The leading negative fringe of the radial near-field profiles indicates the depletion of the local conductivity, $\delta < 0$. To match the amplitude of this fringe (~10%), the depletion has to be significant, $|\delta| \sim 1$.

Our computational method may be suitable for qualitative and quantitative modeling of the near-field response of other spatially inhomogeneous 2D heterostructures. Such applications and details of their implementation will be reported elsewhere.

S4. Ab Initio Calculations of Graphene/α-$RuCl_3$ Heterostructures

The calculations were performed within the Vienna Ab initio Simulation Package (VASP)[16] using a projector-augmented wave (PAW) pseudopotential in conjunction with the Perdew–Burke–Ernzerhof (PBE)[17] functionals and plane-wave basis set with energy cutoff at 400 eV. For the heterostructures with graphene and monolayer α-$RuCl_3$, we used a hexagonal supercell containing 82 atoms (composed of a 5×5 graphene supercell and $\sqrt{3}\times\sqrt{3}$ α-$RuCl_3$ supercell). The resulting strain is ~2.5% for the α-$RuCl_3$ monolayer. For graphene on bilayer α-$RuCl_3$, the model consists of 114 atoms. The surface Brillouin zone was sampled by a 4 × 4 × 1 Monkhorst–Pack k-mesh. A vacuum region of ~15 Å was applied. Because of the absence of strong chemical bonding between layers, van der Waals density functional in the opt88 form[18]

was employed for structural optimization. All structures were fully relaxed until the force on each atom was less than 0.01 eV $Å^{-1}$.

With small Bader charges of 7.01 e (out of 8 e) per orbital, the Ru-4d states cannot be considered fully localized, and therefore, the use of large values of U_{4d} is understood as an ad hoc fitting parameter without physical basis. Instead, each Chlorine 3p orbital charge is 7.34 e (out of 7 e), indicating the importance to employ correction on both Ru and Cl elements. The evaluation of the Hubbard U terms are computed by employing the generalized Kohn–Sham equations within density functional theory including mean-field interactions (DFT+U), as provided by the Octopus package,[19,20] using the ACBN0[21,22] functional together with the local density approximation (LDA) functional describing the semilocal DFT part. We compute ab initio the Hubbard U and Hund's J for the 4d orbitals of Ruthenium and 3p orbital of Chlorine. We employ norm-conserving HGH pseudopotentials to get converged effective Hubbard U values (1.96 eV for Ru and 5.31 for Cl) with spin-orbital couplings.

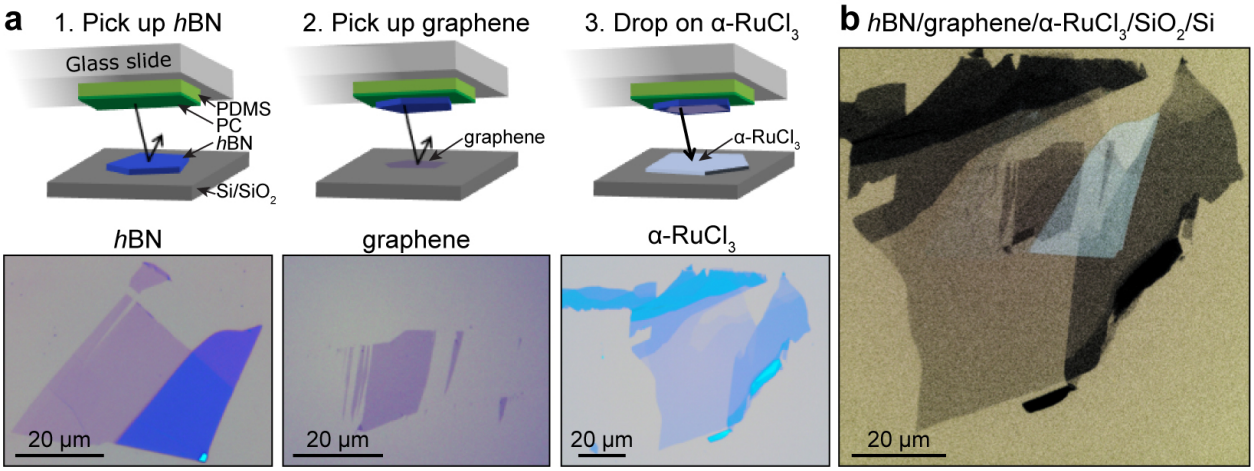

Figure S1. Schematic of assembly for *h*BN/graphene/α-$RuCl_3$/SiO_2/Si. (a) Schematic of the heterostructure assembly. A polycarbonate (PC) film is used to sequentially pick up *h*BN and graphene, which is finally deposited on exfoliated α-$RuCl_3$/SiO_2/Si. (b) Optical image of resulting *h*BN/graphene/α-$RuCl_3$/SiO_2/Si heterostructure.

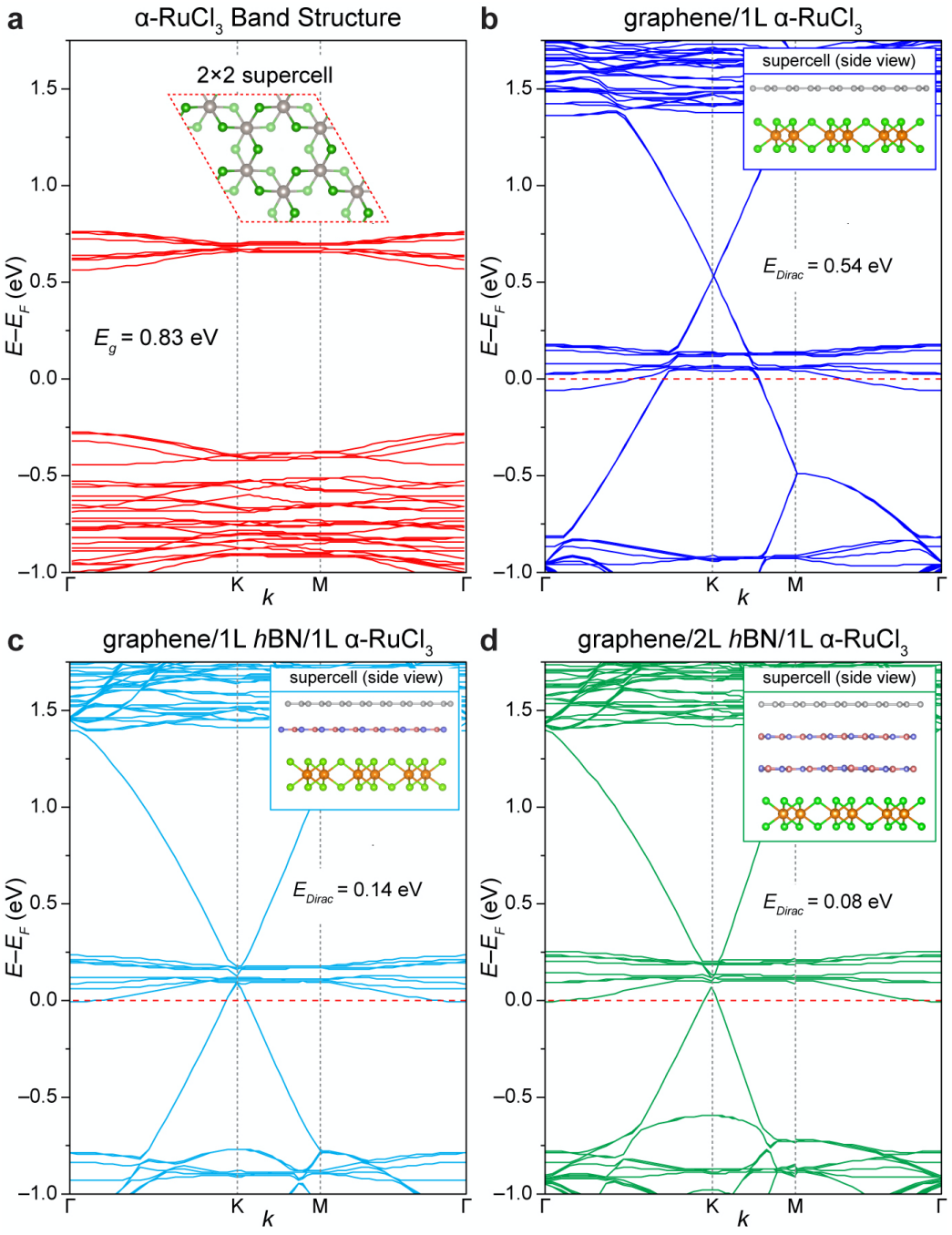

Figure S2. Theoretical electronic structure of freestanding α-$RuCl_3$ and graphene/α-$RuCl_3$ with *h*BN spacers. (a) DFT+U+SOC band structure for 2×2 α-$RuCl_3$ supercell shown in the inset. Our calculations account for different values of the Hubbard U for the Ru 4d and Cl 3p orbitals (U_{4d} = 1.96 eV and U_{3p} = 5.31 eV, respectively), which allows for an accurate description of its band structure. The bandgap of the α-$RuCl_3$ monolayer is 1.07 eV, in excellent agreement with experimental observations (1.2 eV)[23]. (b) Calculated band structure of graphene/α-$RuCl_3$ reproduced from Figure 1c. Band structures with (c) one and (d) two *h*BN spacer layers show an incremental shift in the interlayer charge transfer as indicated by the shift in the Dirac point relative to E_F.

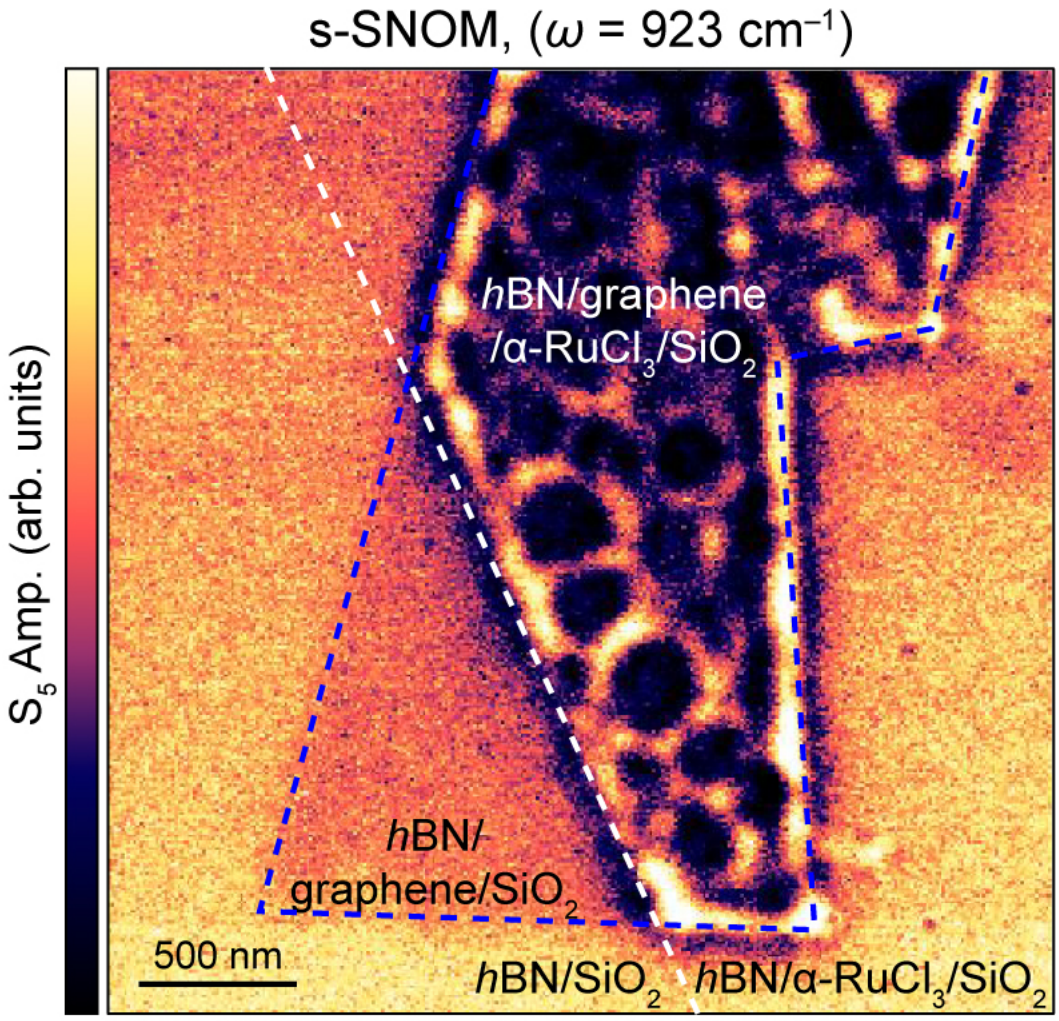

Figure S3. Comparison of Near-field Amplitude of *h*BN/graphene/α-$RuCl_3$/SiO_2 vs. *h*BN/graphene/SiO_2. s-SNOM image ($\omega = 923$ cm^{-1}) of the near-field S_5 amplitude of a piece of graphene that is partially on and off of α-$RuCl_3$. The blue dashed line traces the border of the graphene flake, while the white dashed line traces the edge of α-$RuCl_3$ on an SiO_2 substrate. As is evident from the image, the CPP fringes are only observed for graphene that is in direct contact with α-$RuCl_3$, while the graphene directly on SiO_2 possesses no such fringes.

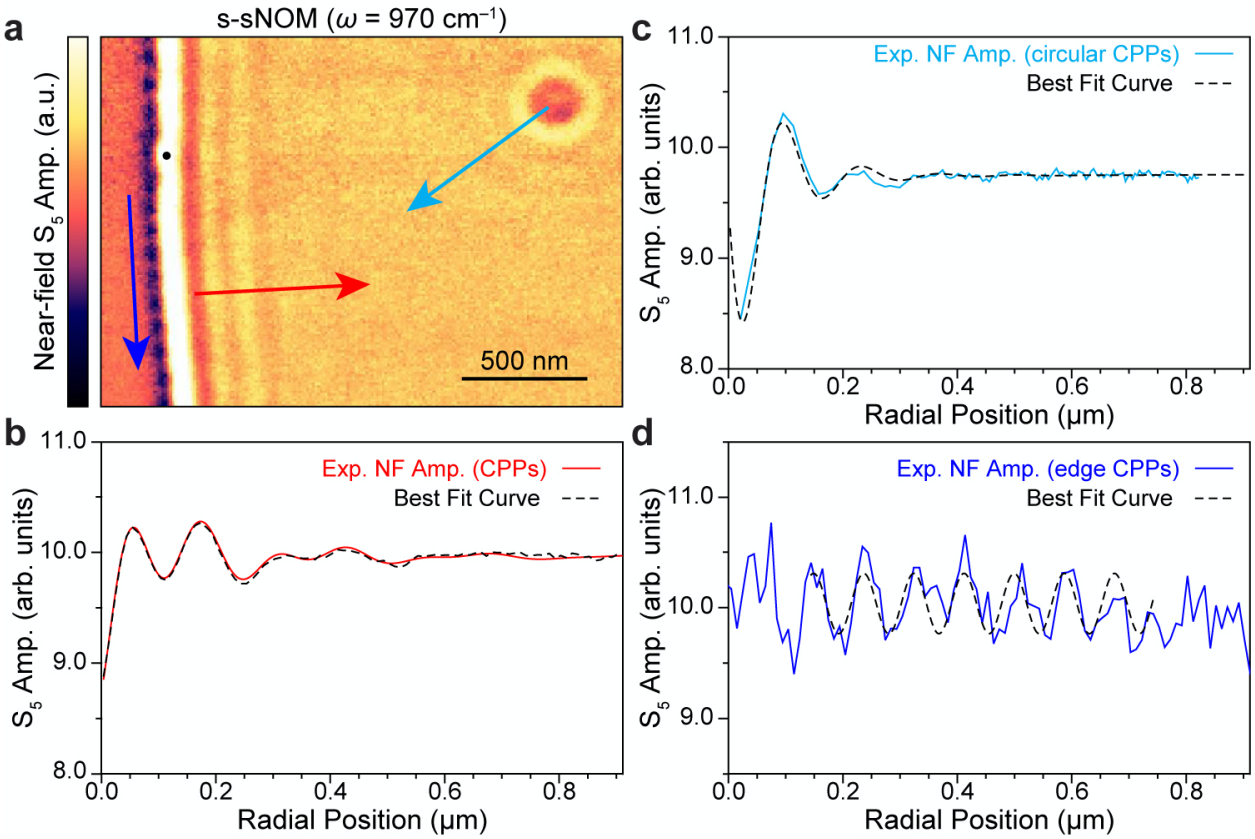

Figure S4. Examples fits to the three types of CPP cross-sections. (a) Map of the near-field S_5 amplitude near a graphene edge ($\omega = 970$ cm^{-1}) showing CPPs (red arrow), circular CPPs (cyan arrow), and edge CPPs (blue arrow). The solid black circle denotes a notch in the graphene edge that is treated as an edge-plasmon reflector. (b) Red line: the average line profile of the near-field amplitude perpendicular to the graphene edge, as shown in (a). Black dashed line: The best-fit curve to the red line using the ansatz presented in [24]: $S_0 + A\frac{e^{-i(q_1+iq_2)x}}{R^a+x^a} + BH_0^{(1)}(2(q_1+iq_2)x)$, where S_0 is the bulk near-field amplitude, R is the approximate tip radius (25 nm), $H_0^{(1)}$ is the first Hankel function of order zero, and q_1 and q_2 are the real and imaginary components of the plasmon wave vector, respectively. (c) Cyan line: the average line profile of the near-field amplitude as a function of radial distance from the center of a point defect. Black dashed line: The best-fit curve to the cyan line assuming only cylindrical components (i.e. only constant and Hankel terms of the equation in (b). (d) Blue line: The average line profile of the near-field amplitude parallel to the graphene edge. Black dashed line: The best fit curve to the blue line using plane-waves. Edge CPP fringes are expected to correspond to $\lambda_p/2$ standing-waves originating from reflection of tip-launched plasmons from notches in the graphene edge, such as that denoted in (a) with a solid black circle.

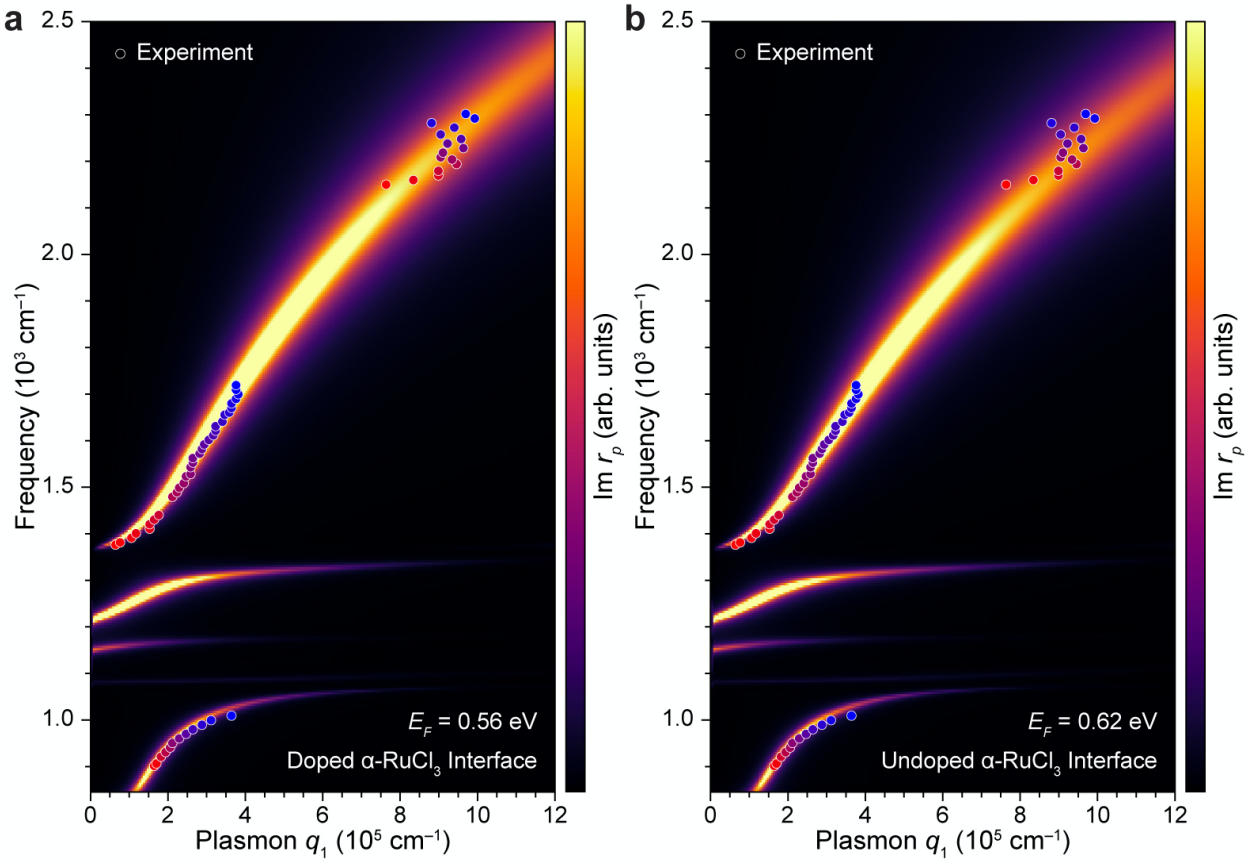

Figure S5. Model CPP dispersions of *h*BN/graphene/α-$RuCl_3$/SiO_2 with and without doped interfacial α-$RuCl_3$. The experimental dispersion from Figure 2c of the main text plotted alongside the best-fit Im r_p calculations based on the experimental stack shown in Figure S8 assuming (a) doped interfacial α-$RuCl_3$ (E_F = 0.56 eV) and (b) undoped interfacial α-$RuCl_3$ (E_F = 0.62 eV). While both (a) and (b) capture the essence of the experimental data, (a) has the best goodness-of-fit.

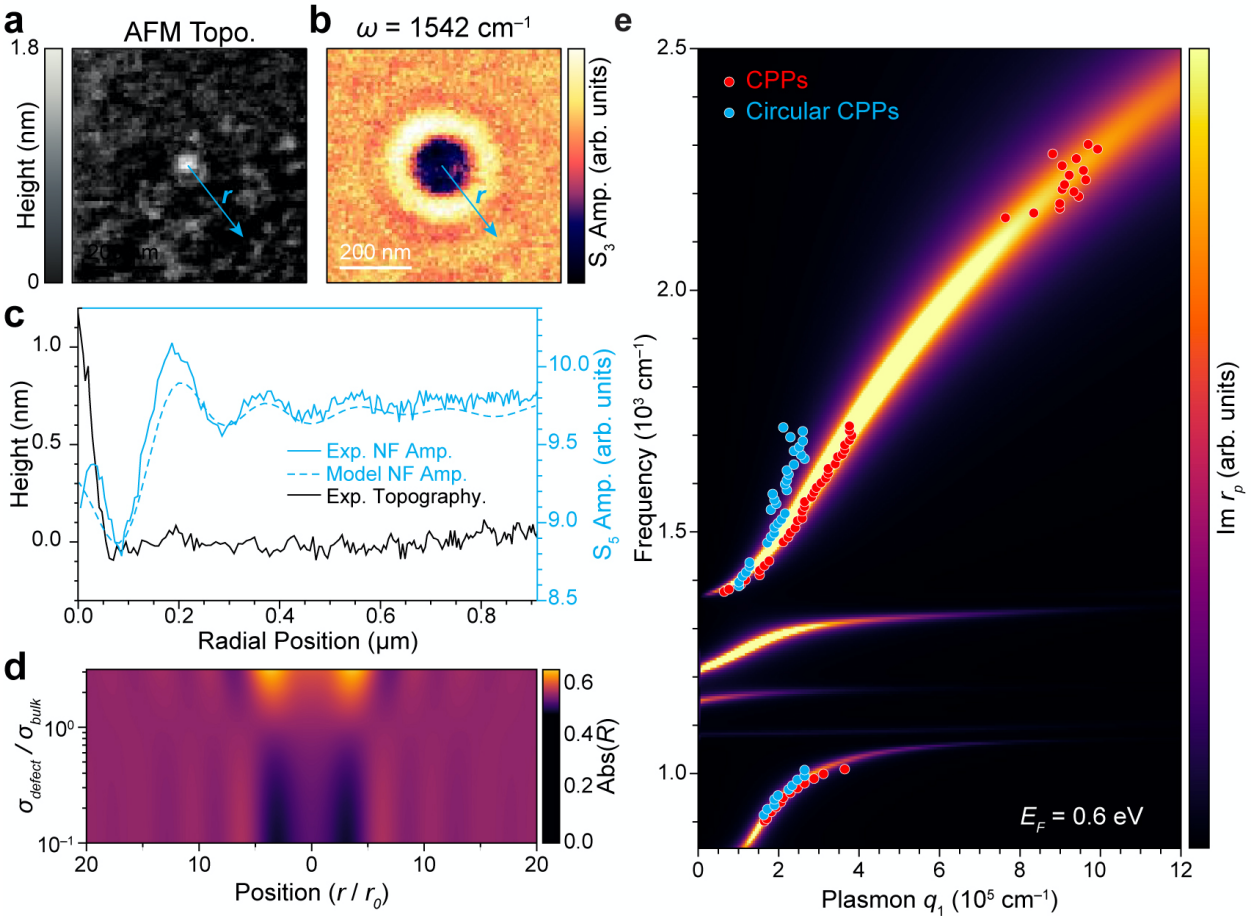

Figure S6. Analysis of circular CPP fringes near point defects in graphene/α-$RuCl_3$ heterostructures. (a) AFM-topography near a topographic point defect. (b) Map of the near-field amplitude (ω = 1542 cm^{-1}) corresponding to the region in (a). (c) Solid cyan curve: Experimental near-field amplitude as a function of radial distance from the topographic point defect for ω = 920 cm^{-1}. Dashed cyan curve: the model fit to the experimental near-field profile based on the assumption of a Lorentzian charge-deficit with r = 40 nm at x = 0. Solid black curve: radial line profile of AFM topography as a function of distance from the center of the defect. (d) Model radial fringe profile as a function of defect conductivity σ_{defect} relative to the graphene bulk. Effective reflectance R of illuminating fields from a dipole-like probe approximate the experimental near-field signal. The sign and magnitude of the first fringe are determined by the magnitude of the defect conductivity relative to that of the bulk. (e) Im r_p and the experimental CPP dispersion (red dots) reproduced from Figure 2c along with the experimental circular CPP dispersion (cyan). While the two experimental dispersions agree well for ω < 1550 cm^{-1}, CPPs at higher frequencies are pushed to lowered q, perhaps due to a nearby resonances in draped debris.

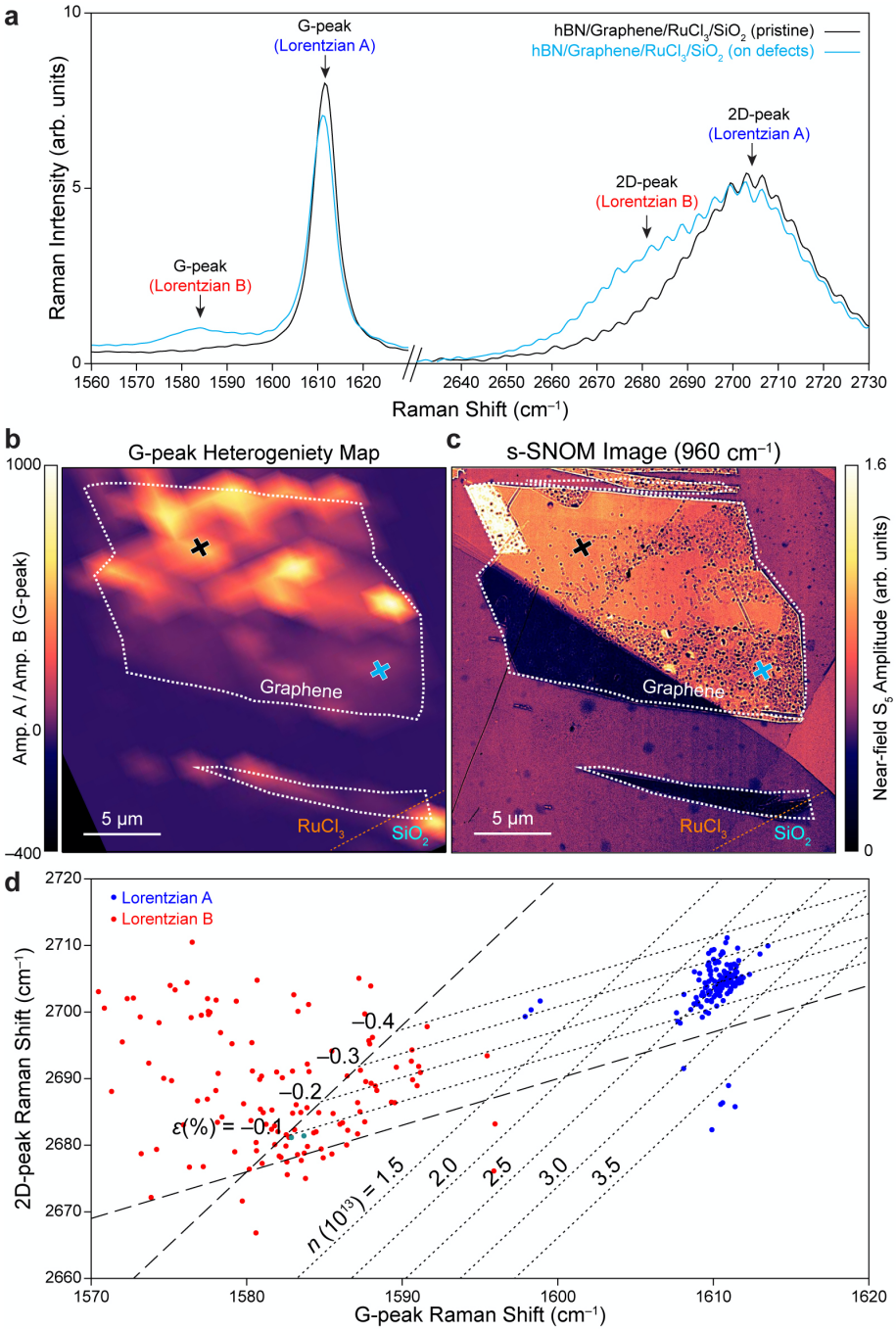

Figure S7. Raman analysis of *h*BN/graphene/α-$RuCl_3$/SiO_2. (a) Raman spectra conducted on graphene with low (black line) and high (cyan line) point defect density. All spectra show a stiffened G and 2D peak (Lorentzian A), and areas with high defect density show additional unshifted G and 2D peaks (Lorentzian B). (b) Spatial dependence of the G-peak heterogeneity showing the ratio of the amplitudes of Lorentzian A to Lorentzian B as defined in (a). (c) Map of the near-field S_5 amplitude over the same region of graphene shown in (b). Areas that show a relative high amplitude for Lorentzian A have a low defect density, while the opposite is true for areas with a high defect density. (d) Plot of the experimental 2D versus G peak Raman shifts shows the co-existence of a uniformly strained, doped phase (blue dots, Lorentzian A), and randomly strained, undoped phase (red dots, Lorentzian B).

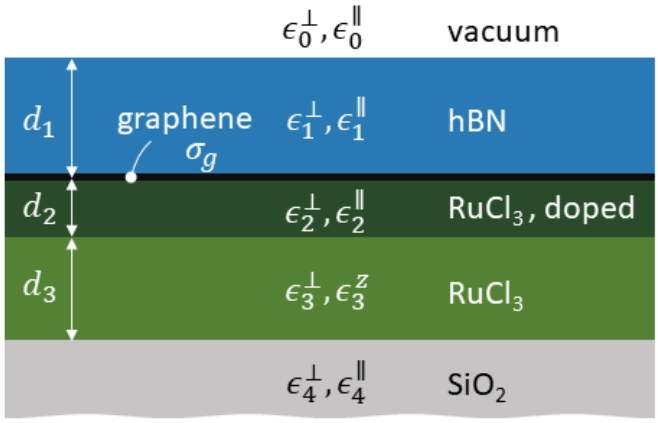

Figure S8. Schematic of the *h*BN/graphene/α-$RuCl_3$/SiO_2/Si heterostructure.

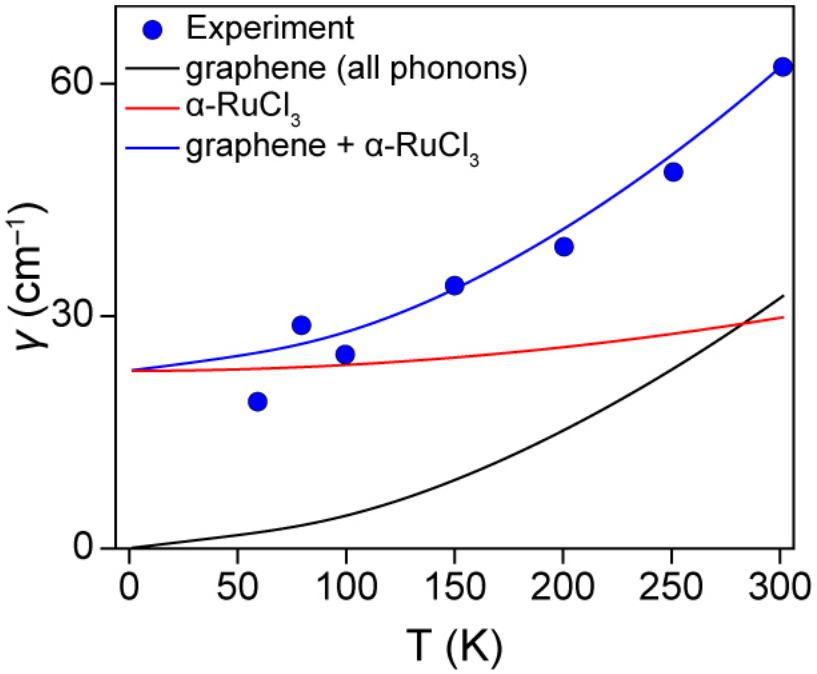

Figure S9. Temperature-dependent scattering in graphene/α-$RuCl_3$. Blue dots: The extracted scattering rate versus temperature derived from the quality factor in Figure 4f of the main text with dielectric losses subtracted. Black line: The model temperature-dependent scattering rate based on graphene phonons only. Red Line: The temperature-dependent contribution of the model interfacial α-$RuCl_3$ layer to the effective scattering rate. Blue line: The total temperature-dependent scattering rate of the graphene and interfacial α-$RuCl_3$ layer.

References

1 Wu, J.-S.; Basov, D. N. & Fogler, M. M. Topological insulators are tunable waveguides for hyperbolic polaritons. *Physical Review B* **2015**, *92*, 205430

2 MATLAB (The MathWorks Inc, Natick, Massachusetts, 2019).

3 Volkov, V. & Mikhailov, S. A. Edge magnetoplasmons: low frequency weakly damped excitations in inhomogeneous two-dimensional electron systems. *Sov. Phys. JETP* **1988**, *67*, 1639-1653

4 Meeker, W. Q. & Escobar, L. A. Teaching about approximate confidence regions based on maximum likelihood estimation. *The American Statistician* **1995**, *49*, 48-53

5 Ruta, F. L.; Sternbach, A. J.; Dieng, A. B.; McLeod, A. S. & Basov, D. N. Quantitative nano-infrared spectroscopy of anisotropic van der Waals materials. *Nano Letters* **2020**

6 Reschke, S.; Mayr, F.; Widmann, S.; Nidda, H.-A.; Tsurkan, V.; Eremin, M.; Do, S.-H.; Choi, K.; Wang, Z. & Loidl, A. Sub-gap optical response in the Kitaev spin-liquid candidate α-$RuCl_3$. *Journal of Physics: Condensed Matter* **2018**, *30*,

7 Caldwell, J. D.; Kretinin, A. V.; Chen, Y.; Giannini, V.; Fogler, M. M.; Francescato, Y.; Ellis, C. T.; Tischler, J. G.; Woods, C. R.; Giles, A. J.; Hong, M.; Watanabe, K.; Taniguchi, T.; Maier, S. A. & Novoselov, K. S. Sub-diffractional volume-confined polaritons in the natural hyperbolic material hexagonal boron nitride. *Nature Communications* **2014**, *5*, 5221

8 Kučírková, A. & Navrátil, K. Interpretation of infrared transmittance spectra of SiO_2 thin films. *Applied spectroscopy* **1994**, *48*, 113-120

9 Ni, G. X.; McLeod, A. S.; Sun, Z.; Wang, L.; Xiong, L.; Post, K. W.; Sunku, S. S.; Jiang, B. Y.; Hone, J.; Dean, C. R.; Fogler, M. M. & Basov, D. N. Fundamental limits to graphene plasmonics. *Nature* **2018**, *557*, 530-533

10 Sohier, T.; Calandra, M.; Park, C.-H.; Bonini, N.; Marzari, N. & Mauri, F. Phonon-limited resistivity of graphene by first-principles calculations: Electron-phonon interactions, strain-induced gauge field, and Boltzmann equation. *Physical Review B* **2014**, *90*, 125414

11 Johnson, R. D.; Williams, S. C.; Haghighirad, A. A.; Singleton, J.; Zapf, V.; Manuel, P.; Mazin, I. I.; Li, Y.; Jeschke, H. O.; Valentí, R. & Coldea, R. Monoclinic crystal structure of α-$RuCl_3$ and the zigzag antiferromagnetic ground state. *Physical Review B* **2015**, *92*, 235119

12 David, B. T.; Young-Duck, Y.; Axel, Z.; Liu, H. L.; Manuel, A. Q.; Moore, S. W.; John, B. G.; Beomhoan, O.; John, T. M.; Ronald, J. K.; Marshall, O. & Cho, J. H. in *Proc.SPIE.*

13 Croft, T. P.; Lester, C.; Senn, M. S.; Bombardi, A. & Hayden, S. M. Charge density wave fluctuations in $La_{2-x}Sr_xCuO_4$ and their competition with superconductivity. *Physical Review B* **2014**, *89*, 224513

14 Rejaei, B. & Khavasi, A. Scattering of surface plasmons on graphene by a discontinuity in surface conductivity. *Journal of Optics* **2015**, *17*, 075002

15 Nikitin, A. Y.; Alonso-González, P.; Vélez, S.; Mastel, S.; Centeno, A.; Pesquera, A.; Zurutuza, A.; Casanova, F.; Hueso, L. E.; Koppens, F. H. L. & Hillenbrand, R. Real-space mapping of tailored sheet and edge plasmons in graphene nanoresonators. *Nature Photonics* **2016**, *10*, 239-243

16 Kresse, G. & Furthmüller, J. Efficient iterative schemes for ab initio total-energy calculations using a plane-wave basis set. *Physical Review B* **1996**, *54*, 11169-11186
17 Perdew, J. P.; Burke, K. & Ernzerhof, M. Generalized gradient approximation made simple. *Physical review letters* **1996**, *77*, 3865
18 Klimeš, J.; Bowler, D. R. & Michaelides, A. Van der Waals density functionals applied to solids. *Physical Review B* **2011**, *83*, 195131
19 Andrade, X.; Strubbe, D.; De Giovannini, U.; Larsen, A.; Oliveira, M.; Alberdi-Rodriguez, J.; Varas, A.; Theophilou, I.; Helbig, N.; Verstraete, M.; Stella, L.; Nogueira, F.; Aspuru-Guzik, A.; Castro, A.; Marques, M. & Rubio, A. Real-space grids and the Octopus code as tools for the development of new simulation approaches for electronic systems. *Phys. Chem. Chem. Phys.* **2015**, *17*,
20 Tancogne-Dejean, N.; Oliveira, M. J. T.; Andrade, X.; Appel, H.; Borca, C. H.; Le Breton, G.; Buchholz, F.; Castro, A.; Corni, S.; Correa, A. A.; De Giovannini, U.; Delgado, A.; Eich, F. G.; Flick, J.; Gil, G.; Gomez, A.; Helbig, N.; Hübener, H.; Jestädt, R.; Jornet-Somoza, J.; Larsen, A. H.; Lebedeva, I. V.; Lüders, M.; Marques, M. A. L.; Ohlmann, S. T.; Pipolo, S.; Rampp, M.; Rozzi, C. A.; Strubbe, D. A.; Sato, S. A.; Schäfer, C.; Theophilou, I.; Welden, A. & Rubio, A. Octopus, a computational framework for exploring light-driven phenomena and quantum dynamics in extended and finite systems. *The Journal of Chemical Physics* **2020**, *152*, 124119
21 Tancogne-Dejean, N.; Oliveira, M. J. T. & Rubio, A. Self-consistent DFT+U method for real-space time-dependent density functional theory calculations. *Physical Review B* **2017**, *96*, 245133
22 Agapito, L. A.; Curtarolo, S. & Buongiorno Nardelli, M. Reformulation of DFT+U as a Pseudohybrid Hubbard Density Functional for Accelerated Materials Discovery. *Physical Review X* **2015**, *5*, 011006
23 Banerjee, A.; Bridges, C. A.; Yan, J. Q.; Aczel, A. A.; Li, L.; Stone, M. B.; Granroth, G. E.; Lumsden, M. D.; Yiu, Y.; Knolle, J.; Bhattacharjee, S.; Kovrizhin, D. L.; Moessner, R.; Tennant, D. A.; Mandrus, D. G. & Nagler, S. E. Proximate Kitaev quantum spin liquid behaviour in a honeycomb magnet. *Nature Materials* **2016**, *15*, 733-740
24 Woessner, A.; Lundeberg, M. B.; Gao, Y.; Principi, A.; Alonso-González, P.; Carrega, M.; Watanabe, K.; Taniguchi, T.; Vignale, G.; Polini, M.; Hone, J.; Hillenbrand, R. & Koppens, F. H. L. Highly confined low-loss plasmons in graphene–boron nitride heterostructures. *Nature Materials* **2015**, *14*, 421-425